Received: 23 May 2022 | Accepted: 29 October 2022

DOI: 10.1111/1462-2920.16275

RESEARCH ARTICLE

environmental microbiology Applied Microbiology International

Transport-limited reactions in microbial systems

Stilianos Louca[1,2] | Gordon T. Taylor[3] | Yrene M. Astor[4] | Kristen N. Buck[5] | Frank E. Muller-Karger[5]

[1]Department of Biology, University of Oregon, Oregon, USA

[2]Institute of Ecology and Evolution, University of Oregon, Oregon, USA

[3]School of Marine and Atmospheric Sciences, Stony Brook University, New York, New York, USA

[4]Estación de Investigaciones Marinas de Margarita, Fundación La Salle de Ciencias Naturales, Punta de Piedras, Estado Nueva Esparta, Venezuela

[5]College of Marine Science, University of South Florida, Florida, USA

Correspondence
Stilianos Louca, Department of Biology, University of Oregon, USA.
Email: louca.research@gmail.com

Funding information
Alfred P. Sloan Foundation; National Aeronautics and Space Administration; Simons Foundation; US National Science Foundation; Fundación La Salle de Ciencias Naturales de Venezuela (FLASA); Estación de Investigaciones Marinas de Margarita (FLASA/EDIMAR); R/V Hermano Ginés (FLASA); Consejo Nacional de Ciencia y Tecnología, Grant/Award Number: 96280221; Fondo Nacional de Ciencia, Tecnología e Investigación, Grant/Award Numbers: 2011000353, 2000001702; Ley de Ciencia, Tecnología e Innovación, Grant/Award Number: 23914; National Science Foundation, Grant/Award Numbers: OCE-0326313, OCE-0963028, OCE-0326268, OCE-9711318, OCE-9415790, OCE-9729697, OCE-491 9401537, OCE-9729284, OCE-9216626, OCE-0752139, 1259110, 0752014, 0326175, 0118491, 9730278, 9711318; NASA, Grant/Award Numbers: NNX14AP62A, NAS5-97128, NAG5-6448; Inter-American Institute for Global Change Research, Grant/Award Number: IAI-CRN3094

Abstract

Predicting microbial metabolic rates and emergent biogeochemical fluxes remains challenging due to the many unknown population dynamical, physiological and reaction-kinetic parameters and uncertainties in species composition. Here, we show that the need for these parameters can be eliminated when population dynamics and reaction kinetics operate at much shorter time scales than physical mixing processes. Such scenarios are widespread in poorly mixed water columns and sediments. In this 'fast-reaction-transport' (FRT) limit, all that is required for predictions are chemical boundary conditions, the physical mixing processes and reaction stoichiometries, while no knowledge of species composition, physiology or population/reaction kinetic parameters is needed. Using time-series data spanning years 2001–2014 and depths 180–900 m across the permanently anoxic Cariaco Basin, we demonstrate that the FRT approach can accurately predict the dynamics of major electron donors and acceptors (Pearson $r \geq 0.9$ in all cases). Hence, many microbial processes in this system are largely transport limited and thus predictable regardless of species composition, population dynamics and kinetics. Our approach enables predictions for many systems in which microbial community dynamics and kinetics are unknown. Our findings also reveal a mechanism for the frequently observed decoupling between function and taxonomy in microbial systems.

INTRODUCTION

Microbial metabolism shapes the biogeochemistry and overall productivity in marine and freshwater systems. Oxygen-deficient 'dead zones' in the ocean, for example, result from microbial respiration processes driving O_2 concentrations below the tolerance thresholds of most eukaryotes (Carstensen et al., 2014; Diaz & Rosenberg, 2008; Wright et al., 2012). In such zones, microbial redox pathways used for energy, such as denitrification, anammox, sulfide oxidation, and dissimilatory nitrate reduction to ammonium (DNRA), control

© 2022 Applied Microbiology International and John Wiley & Sons Ltd.

14622920, 0, Downloaded from https://sfamjournals.onlinelibrary.wiley.com/doi/10.1111/1462-2920.16275 by University Of Oregon, Wiley Online Library on [21/11/2022]. See the Terms and Conditions (https://onlinelibrary.wiley.com/terms-and-conditions) on Wiley Online Library for rules of use; OA articles are governed by the applicable Creative Commons License

nitrogen, sulfur and carbon fluxes, with implications for global marine productivity and climate (Lam et al., 2009; Ulloa et al., 2012). In marine sediments, microbes control the production and consumption of methane, an important greenhouse gas. Modelling these processes remains a hard problem, due to the incredible diversity and complexity of microbial communities, uncertainties regarding the growth- and reaction-kinetic parameters of each species, and limited knowledge of local species compositions needed for constraining kinetic parameters. Indeed, the few existing realistic biogeochemical and microbial system models suffer from a dependence on dozens or even hundreds of microbial kinetic parameters (Louca, Hawley, et al., 2016; Oguz et al., 2000; Reed et al., 2014; Yakushev, 2013) that define microbial population dynamics and metabolism. These complexities and parameter uncertainties are a major reason why most ocean biogeochemical models and Earth system models tend to only coarsely divide the microbial compartment into photosynthesizers ('phytoplankton'), zooplankton and detritivores (Aumont et al., 2015; Coles & Hood, 2016; Vichi et al., 2020), thus ignoring many important microbial redox pathways. There is thus a need for properly simplified models that focus on the subset of factors that limit biogeochemical process rates, in other words models that identify and properly 'shortcut' the factors that may not actually be rate limiting.

In many systems, such as poorly mixed water columns or sediments, microbial growth- and reaction-kinetics tend to operate at much shorter time scales than physical transport or mixing of reactants across space. For example, in some ocean regions the expected travel times of dissolved nutrients across geochemical gradients are in the order of months to years (see e.g. Supplement S.5 or Louca, Astor, et al., 2019) and thus much longer than typical microbial doubling times (e.g. observed in batch incubations) and substrate half-life-times (when no other substrate is limiting), which tend to be in the order of days or less (Gibson et al., 2018; Hordijk et al., 1985; Louca, Hawley, et al., 2016; Sonne-Hansen et al., 1999; van Bodegom & Scholten, 2001). In such situations, the maximum rate at which reactants can possibly be transported from their locations of production to their locations of consumption is expected to become the limiting factor for bulk (i.e. summed over all organisms) metabolic rates (Louca, Scranton, et al., 2019). This expectation is supported by ecological theory, which predicts that given sufficient time local communities will tend to be dominated by organisms that can survive at low substrate concentrations (Tilman, 1982), at which point the rates of substrate consumption become limited by the rates of substrate influx from their location of origin to their location of consumption. This situation is conceptually analogous to diffusion-limited enzymatic reactions, where enzymes are so efficient that diffusion (at the micro-scale) to their active sites is the rate-limiting step (Alberty & Hammes, 1958; Debnath et al., 2019). As we argue below, this separation of time scales between microbial kinetics and mixing across space should make it possible to design substantially simplified dynamical models that accurately predict the rates of 'fast' dissimilatory metabolic reactions while short-cutting the underlying microbial kinetics. To date, this idea remains largely untested for microbially driven processes, especially in marine and lake systems.

We present a new class of stoichiometrically, thermodynamically and hydrodynamically consistent biogeochemical models, henceforth "fast-reaction-transport" (FRT) models, that exploit the aforementioned separation of time scales between mixing and fast metabolic reactions, thus eliminating the need for kinetic parameters involved in microbial growth and metabolism. These models only require knowledge of a system's physical transport processes (e.g. hydrodynamics, diffusion coefficients, etc), chemical boundary conditions (e.g. the concentrations or fluxes of substrates at the top and bottom of a water column) and the stoichiometry of the reactions; note that this information is generally required for any biogeochemical model. If accurate, FRT models would drastically facilitate biogeochemical modelling for many marine systems, since they substantially reduce the number of required parameters and allow predictions in situations where microbial species compositions and kinetics are highly uncertain. We discuss similarities to, and important advantages over, previous models that exploit a similar separation of time scales, and we provide easily understandable illustrations of the expected dynamics. To test the applicability of FRT models in realistic situations, we consider the microbially driven biogeochemistry in the water column of the Cariaco Basin (depths 180–900 m), the largest and best studied permanently anoxic truly marine basin in the world (Muller-Karger et al., 2019; Scranton et al., 2014), and compare the model to 14 years of chemical time-series data. We find that the FRT model accurately predicts the system's major redox structure and fluxes of all considered compounds across hundreds of meters, with absolutely no consideration of the local species composition or kinetic properties.

RESULTS AND DISCUSSION

The fast-reaction-transport limit

Most reaction-transport models for microbially driven biogeochemistry (Aumont et al., 2015; Coles & Hood, 2016; Preheim et al., 2016; Vichi et al., 2020; Yakushev, 2013) can essentially be formulated as partial differential equations of the form:

14622920, 0, Downloaded from https://sfamjournals.onlinelibrary.wiley.com/doi/10.1111/1462-2920.16275 by University Of Oregon, Wiley Online Library on [21/11/2022]. See the Terms and Conditions (https://onlinelibrary.wiley.com/terms-and-conditions) on Wiley Online Library for rules of use; OA articles are governed by the applicable Creative Commons License

$$\frac{\partial C_m}{\partial t} = \underbrace{\sum_r \mathbb{S}_{mr} h_r}_{\text{microbial reactions}} + \underbrace{\nabla \cdot (\mathbb{D}_m \nabla C_m - \mathbf{v}_m C_m)}_{\text{physical transport}}, \quad (1)$$

where C_m is the concentration of the mth chemical substance (mol · L^{-1}) in any given time and location, t is the time, r iterates over all reactions, h_r is the rate of reaction r at any given time and location (mol · L · d^{-1}), $\mathbb{S}_{mr}$ is the stoichiometric coefficient of substance m in reaction r (Resendis-Antonio, 2013), ∇ is the Nabla spatial differential operator (essentially taking partial derivatives of its right side with respect to all spatial dimensions), $\mathbb{D}_m$ is the diffusivity matrix describing the diffusion-like dispersal of the m-th substance (for one-dimensional models $\mathbb{D}_m$ is a scalar) and $\mathbf{v}_m$ is a vector representing advection velocities (e.g. due to water currents or particle sinking). The reaction rate h_r depends on the concentrations of one or more substances according to some rate law, for example, a mass action law:

$$h_r = \kappa_r \prod_{m \in L_r} C_m, \quad (2)$$

where κ_r is a kinetic parameter and L_r denotes the set of all substrates for reaction r (other rate laws, e.g. of Monod type, or with inhibitions, are also common). In many models h_r is also modulated by a thermodynamic driving force that is zero when the reaction is endergonic (Jin & Bethke, 2007; Louca, Hawley, et al., 2016; Reed et al., 2014). The concentrations C_m and reaction rates h_r vary with time and space, while $\mathbb{D}_m$, $\mathbf{v}_m$ and κ_r may or may not be time- and space-dependent. In more complex models accounting for microbial population dynamics, κ_r itself scales with the population density of the involved microorganisms, whose population dynamics may themselves be described by additional differential equations (Louca, Hawley, et al., 2016; Yakushev, 2013).

The FRT framework proposed here formally corresponds to the limit were the coefficients κ_r (in the case of mass-action kinetics) or the maximum reaction rates (in the case of Monod kinetics) approach infinity while the $\mathbb{D}_m$ and $\mathbf{v}_m$ remain finite. In this limit, reactions can proceed infinitely fast when substrates are abundant, which however is not sustainable except for a negligibly (infinitesimally) short period due to the finite rates of substrate transport across space. In practice, this limit is approached when the hypothetical half-lifetime of each substrate consumed by a reaction (when no other substrate is limiting) is much shorter than the expected time it takes for individual molecules to travel distances typical for the system's chemical gradients (detailed discussions in Supplements S.6 and S.7), and much shorter than the time scales over which a system's boundary conditions change. A similar separation of time scales has been considered previously for fast abiotic reversible reactions, such as acid-dissociation reactions, in groundwater models (Goddard, 1990; Lichtner, 1985; Rubin, 1983). These models, known as 'equilibrium-reaction-transport' (ERT) models, assume that reactions are reversible and so fast (in both directions) that they are always at local thermodynamic equilibrium. The assumption of thermodynamic equilibrium means that a subset of the differential equations in Equation (1) can be replaced by algebraic ones, which are solved together with the remaining differential equations. While ERT models have proven successful for modelling abiotic reaction systems (Rasilainen et al., 1999; Zhang et al., 2007), they are unsuitable for microbial systems, because many microbially driven reactions are not reversible within the typical time scales considered and thus are not guaranteed to be at equilibrium even if they exhibit infinitely fast kinetics in one direction (detailed explanation in Supplement S.1). This is especially important for reactions with standard ΔG close to 0, since such reactions may be thermodynamically favoured in either direction depending on environmental conditions. For example, anaerobic ammonia oxidation (anammox, $NH_4^+ + NO_2^- \rightarrow N_2 + 2H_2O$) is catalyzed by multiple species (Kartal et al., 2012; Sonthiphand et al., 2014); however, no organism is known capable of catalysing its reverse, even when thermodynamically favourable. Assuming instantaneous reversibility of anammox could thus lead to drastically unrealistic predictions (see Figure S2 for an example). There is thus a need for a more general framework that does not assume reversibility of reactions but still separates the time scales of reaction kinetics and transport. A special case of such a framework was recently introduced by Louca, Scranton, et al. (2019). However, that framework was fundamentally restricted to steady-state situations, which most natural microbial systems do not satisfy. In contrast, the FRT approach that we present below can handle dynamics far from steady state and can include unidirectionally catalyzed reactions. In addition, as will become apparent below, our suggested numerical approach is substantially simpler to implement that ERT models, which require the treatment of a differential-algebraic system of equations.

We emphasize that reaction-transport models accounting for reaction kinetics and/or microbial population dynamics are generally more realistic and in principle expected to outperform FRT models, if all kinetic parameters were accurately known (which is rarely the case). The question is thus not whether a properly parameterized kinetic model is more accurate than a much simpler FRT model, but whether in some situations FRT models alone already provide a sufficiently

14622920, 0, Downloaded from https://sfamjournals.onlinelibrary.wiley.com/doi/10.1111/1462-2920.16275 by University Of Oregon, Wiley Online Library on [21/11/2022]. See the Terms and Conditions (https://onlinelibrary.wiley.com/terms-and-conditions) on Wiley Online Library for rules of use; OA articles are governed by the applicable Creative Commons License

accurate description of certain biogeochemical processes.

Numerical implementation

Reaction-transport models such as the ones in Equation (1) can be numerically simulated in the FRT limit as follows (for pseudocode, see Supplement S.2). We henceforth discretize space and time as is usual in finite difference schemes. To achieve the FRT limit numerically, we split each time step into two stages, a 'transport' stage in which solely the transport dynamics are simulated for a small time interval δ while keeping reactions 'frozen', and a 'fast reaction' stage in which the reactions are simulated in each spatial grid cell until convergence and while keeping the transport dynamics and real time frozen (Figure 1). During the fast reaction stage, we assume that each spatial grid cell is a well-mixed isolated microscopic box, that reactions only occur when they are exergonic (i.e. free energy yielding, $\Delta G < 0$), and that reactions proceed until reaching a state where no reaction is exergonic anymore, henceforth called 'dead end'. The assumption that a redox reaction is only biologically catalyzed if it is exergonic largely applies to dissimilatory reactions performed by microbes for energy (Canfield & Thamdrup, 2009), as is the case for all reactions considered here. Note that, in contrast to ERT models, reactions do not necessarily need to be at perfect equilibrium in order for a dead end to be reached, as long as all reactions are no longer exergonic. Time units in the fast reaction stage are considered infinitely smaller than real time units, and thus real time is only advanced during the transport stage. Note that the particular trajectory followed within a single spatial grid cell during a fast reaction stage is irrelevant, since during the fast reaction stage real time is frozen and hence all that matters is the dead end reached in each grid cell at the end of that fast reaction stage. For sufficiently short time steps δ, that is, sufficiently frequent fast reaction stages, this implementation converges to the FRT limit. Using the above implementation, it is also straightforward to estimate net rates of production/consumption for the involved chemical substances, by calculating the difference between their concentrations before and after each fast reaction stage, and dividing that difference by the time step δ.

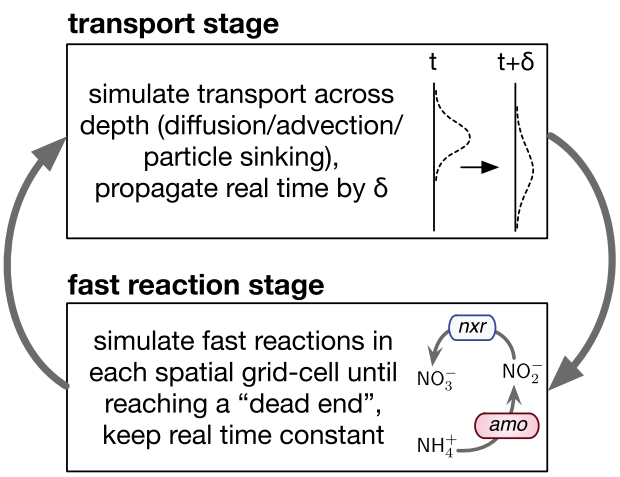

FIGURE 1 Schematic of a single numerical iteration of an FRT model defined along a, consisting of two interleaved stages. During the transport stage, real time is advanced and physical transport processes (e.g. eddy diffusion) as well as any slow (kinetically limited) reactions are integrated. During the fast reaction stage, real time is held constant and fast reactions are integrated in each spatial grid cell until a dead end is reached, that is, until all fast reactions are non-exergonic. For pseudocode, see Supplement S.2.

To ensure that a dead end is reached in short computing time in each spatial grid cell during the fast reaction stage and to avoid any need for kinetic parameters, in the implementation presented here each catalyzed reaction simply proceeds at a rate proportional to its distance from thermodynamic equilibrium, and only while it is exergonic (rate $\propto -\Delta G$, as long as $\Delta G < 0$, details in Supplement S.3). To increase biological realism, it is also possible to impose a non-zero threshold on the free energy that must be available from a reaction in order for it to be biologically catalyzed. Indeed, it has been argued that various metabolic reactions should halt when their ΔG is above a certain 'energy quantum' or critical free energy value, which typically ranges from -20 to -10 kJ $\cdot$ mol^{-1} (Hoehler, 2004; Schink, 1997) (although syntrophic associations can push this threshold close to zero; Jackson & McInerney, 2002). That said, in both of our example simulations and in our Cariaco Basin model, discussed below, we saw no substantial effects of such a biological energy quantum on the simulation outcomes, when tested in the range -20 to 0 kJ $\cdot$ mol^{-1}. Note that the above thermodynamics-based rate laws during the fast reaction stage are largely motivated by numerical convenience (e.g. they ensure rapid convergence to a dead-end) and biological plausibility; however, other choices are also possible. Indeed, one can easily implement other rate laws in the fast reaction stage (e.g. mass action kinetics as in Equation (2)), as long as reactions are simulated until reaching a dead end and without advancing real time. Through extensive simulation tests, including with the Cariaco Basin model discussed below, we found that the effects of such alternative choices on the overall outcome were negligible (details in Supplement S.4).

We point out that for systems exhibiting both fast (not kinetically limited) and slow (i.e. kinetically limited) reactions, such as slow organic carbon degradation reactions or oxygenic photosynthesis, the slow reactions can simply be integrated during the transport stage with appropriate kinetic laws, as is already done in existing software. The proposed approach can be incorporated in most biogeochemical and ocean modelling codes (Aumont et al., 2015; Coles & Hood, 2016;

14622920, 0, Downloaded from https://sfamjournals.onlinelibrary.wiley.com/doi/10.1111/1462-2920.16275 by University Of Oregon, Wiley Online Library on [21/11/2022]. See the Terms and Conditions (https://onlinelibrary.wiley.com/terms-and-conditions) on Wiley Online Library for rules of use; OA articles are governed by the applicable Creative Commons License

Vichi et al., 2020), including codes with variable time steps and irregular spatial grids, by interleaving the standard integration step with the FRT's fast reaction stage wherever some reactions are expected to be transport limited. Since FRT models can easily also include fast abiotic (reversible) reactions, they cover classical ERT models as a special case. In practice, fast reversible reactions may either be explicitly fixed at equilibrium during the fast reaction stage (i.e., as algebraic constraints), or simply represented by two separate fast irreversible reactions (one for each direction).

Simple examples

To illustrate the types of dynamics expected in the FRT limit, we consider two simple hypothetical systems of microbially catalyzed redox reactions, in a poorly mixed water column and a sediment column, respectively. For simplicity, we assume lateral homogeneity, and thus consider only a single spatial dimension representing depth. In the first example, we consider the oxidation of hydrogen sulfide diffusing upwards from the sediments with oxygen diffusing downwards from the euphotic zone ($H_2S + 2O_2 \rightarrow SO_4^{2-} + 2H^+$) (Li et al., 2012). Simulating the dynamics of this reaction-transport system in the FRT limit only requires us to specify boundary concentrations of H_2S and O_2 (at the top and bottom of the water column), their initial concentrations (if we care about early transients), the reaction stoichiometry, the diffusivities and advection rates. We assume that physical transport of all substances is driven solely by eddy diffusion with a constant diffusivity $\mathbb{D}$, set to the typical diffusivity in Cariaco Basin at 300 m depth (Louca, Astor, et al., 2019). We are interested in how the H_2S and O_2 profiles and fluxes evolve over time, following an initial 'flush' or deep-water renewal, where oxygen-rich surface water mixes into the entire water column, and thus initialize H_2S to zero and O_2 to its upper boundary value (160 μM). As seen in Figure 2A–C, a

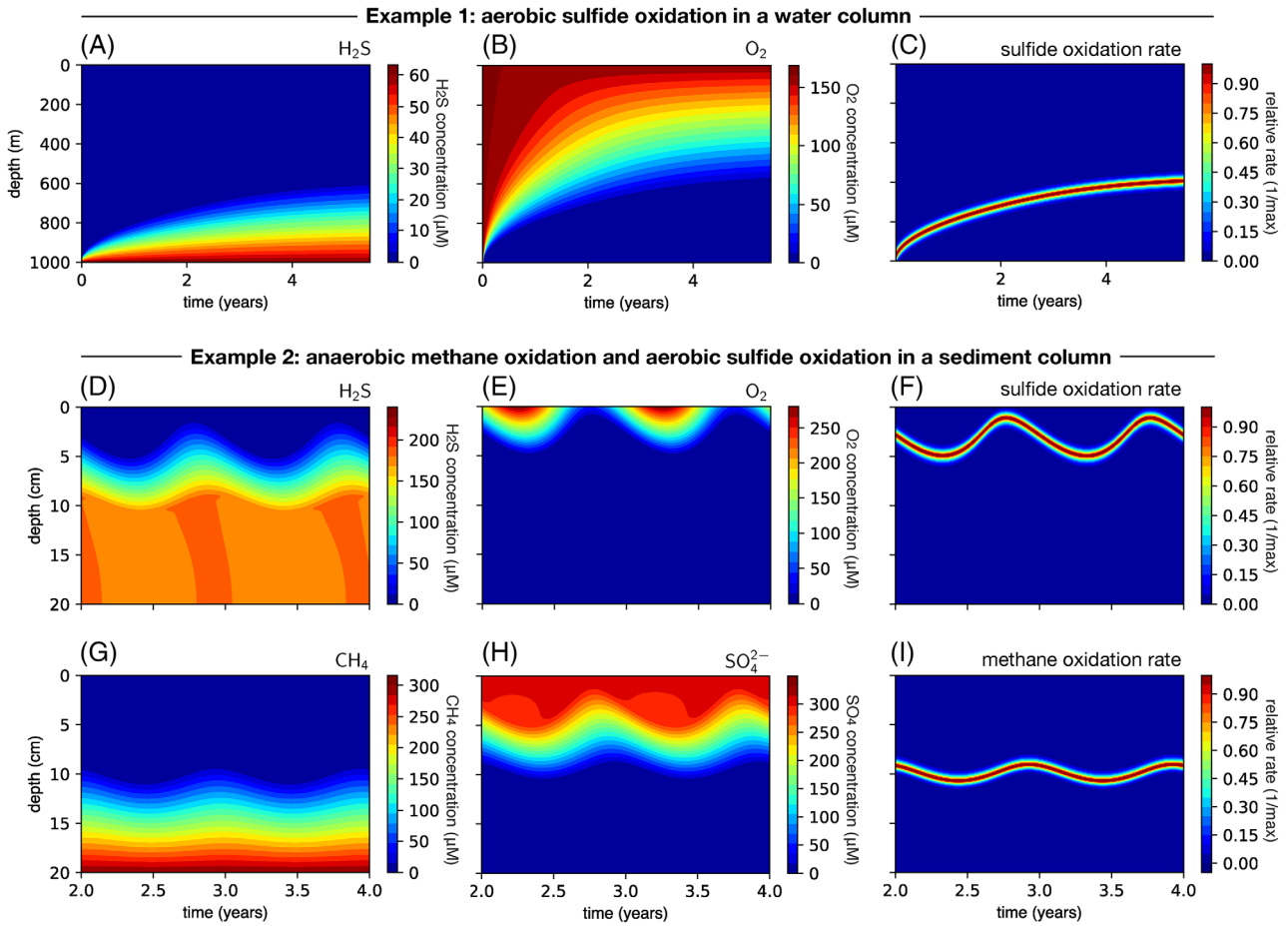

FIGURE 2 Example dynamics. Hypothetical examples of dynamics expected for biogeochemical reaction-transport systems in the FRT limit, where reaction kinetics are much faster than physical transport rates. (A–C, Example 1): Aerobic oxidation of H_2S in a poorly mixed water column, following an initial deep water renewal. (A) and (B) show predicted H_2S and O_2 concentrations, respectively; (C) shows the reaction rate profile relative to the maximum rate at any depth (i.e. at each time point normalized to maximum 1, to emphasize the location of the migrating reaction front). (D–I, Example 2): Aerobic oxidation of H_2S and SO_4^{2-}-dependent anaerobic oxidation of CH_4 in a sediment column, with seasonally varying O_2 concentrations at the top boundary. Only the long-term periodic response to the seasonal forcing is shown, omitting the initial transient. For 'snapshot' depth profiles of predicted concentrations at specific times see supplemental Figure S1.

14622920, 0, Downloaded from https://sfamjournals.onlinelibrary.wiley.com/doi/10.1111/1462-2920.16275 by University Of Oregon, Wiley Online Library on [21/11/2022]. See the Terms and Conditions (https://onlinelibrary.wiley.com/terms-and-conditions) on Wiley Online Library for rules of use; OA articles are governed by the applicable Creative Commons License

sharp reaction front (i.e. a narrow H_2S–O_2 interface) quickly forms, which then slowly migrates upwards and eventually stabilizes at some intermediate depth; this final depth is the unique depth at which steady-state H_2S and O_2 fluxes are consistent with the reaction stoichiometry (Louca, Scranton, et al., 2019). Despite the fast reaction kinetics, the reaction front only migrates slowly and the system takes years to converge to its steady state due to the slow physical transport. Sharp reaction fronts are also known from ERT models (Lichtner, 1985; Neretnieks, 1993) and are widely observed in natural systems with low mixing rates, such as poorly mixed water columns (Brettar & Rheinheimer, 1991; Gies, 2015; Hannig et al., 2007; İnceoğlu et al., 2015; Lam et al., 2007; Li et al., 2012; Louca, Hawley, et al., 2016; Murray et al., 1989; Sorokin et al., 2007), sediments (Boudreau, 1991; Canfield & Thamdrup, 2009; Iversen & Jorgensen, 1985; Roque & Petroff, 2022; Treude et al., 2005) and microbial mats (Stewart & Franklin, 2008). Fluxes of electron donors and acceptors into these reaction fronts typically fuel intense microbial metabolic rates and growth (Brettar & Rheinheimer, 1991; Grote et al., 2008; Indrebo et al., 1979; Lehours et al., 2005; Louca, Hawley, et al., 2016; Taylor et al., 2001; Treude et al., 2005; Wenk et al., 2013; Zaikova et al., 2010; Zubkov et al., 1992).

In the second example, we consider two microbially catalyzed coupled redox reactions in a freshwater sediment column: sulfate-dependent anaerobic oxidation of methane ($CH_4 + SO_4^{2-} + 2H^+ \rightarrow H_2S + CO_2 + 2H_2O$) (Deutzmann, 2020; Mostovaya et al., 2022) and aerobic oxidation of sulfide ($H_2S + 2O_2 \rightarrow SO_4^{2-} + 2H^+$), with methane originating from deeper sediment layers, oxygen originating from the water column, and H_2S and SO_4^{2-} acting as temporary intermediates ("electron shuttles") between the two reactions. We assume that transport occurs exclusively via molecular diffusion, with diffusivities for each substance taken from the literature (see Experimental Procedures for details). We are interested in the system's response to seasonal variations in oxygen concentrations at the water–sediment interface, and hence we set the O_2 concentration at the top boundary to a sinusoidally oscillating function of time, while keeping the boundary concentrations of all other substances constant. Further, we first simulate the system for 1 year to allow convergence toward its long-term periodic trajectory. As initial condition we assume a recently mixed sediment column similar to Example 1 (i.e. a constant non-zero O_2 and SO_4^{2-} profile between the top and bottom boundary, with methane and sulfide absent), although we mention that the precise initial condition had no influence on the system's long-term trajectory. As seen in Figure 2D–I, two separated sharp reaction fronts quickly emerge, one for sulfide oxidation near the sediment–water interface and one for methane oxidation several centimetres deeper. Between the two fronts, an upward flux of H_2S and a downward flux of SO_4^{2-} provide necessary electron donors and acceptors, respectively, to the two reactions. The model qualitatively reproduces the spatial structure seen in many freshwater and marine sediments (Mostovaya et al., 2022; Niewöhner et al., 1998; Treude et al., 2005), although we mention that in reality many additional electron donors/acceptors tend to be involved (Canfield & Thamdrup, 2009). The seasonal variation in boundary oxygen concentrations drives a periodic response in the location and intensity of both reaction fronts. However, due to the slow diffusive transport this response occurs at delays of multiple months, causing phase shifts in the reaction fronts' oscillations relative to the driving force, especially in the deeper methane-oxidizing front.

Both of the above examples suggest that the FRT limit leads to relatively simple dynamics that are largely driven by the system's boundary conditions, although long-lasting transients may be observed following perturbation when transport rates are particularly slow. Indeed, in the first example the reaction front's location and activity rate eventually stabilize after several years, while in the second example the observed oscillations are entirely driven by the seasonally changing boundary conditions. In our estimate, it is unlikely that oscillations or other rich dynamics could be sustained indefinitely in the FRT limit when boundary conditions (and model parameters such as $\mathbb{D}_m$ and $\mathbf{v}_m$) are constant, although additional numerical explorations are needed to more confidently rule out this possibility.

A realistic FRT model for the Cariaco Basin

To test the applicability of the FRT limit to realistic microbial systems, we constructed an FRT model for the Cariaco Basin water column, depths 180–900 m. The model describes the spatiotemporal dynamics of multiple dissolved substances involved in microbial energy metabolism, and transported across space via turbulent (eddy) diffusion. Since lateral transport in the Cariaco Basin is generally much faster than vertical transport, we assume lateral homogeneity, consistent with previous models for this system (Li et al., 2012; Louca, Astor, et al., 2019; Louca, Scranton, et al., 2019; Scranton et al., 1987). The model thus exhibits a single spatial dimension representing depth, though it accounts for changes in the basin's lateral surface area with depth (details in Experimental Procedures). Estimated diffusive travel times across this zone are in the order of months to years (Supplement S.5) and thus much longer than typical microbial doubling times or substrate half-life-times under non-limiting conditions. Our model focuses on microbially catalyzed reactions thought to be largely responsible for the nitrogen and sulfur cycles in the oxygen-deficient part of the Cariaco

14622920, 0, Downloaded from https://sfamjournals.onlinelibrary.wiley.com/doi/10.1111/1462-2920.16275 by University Of Oregon, Wiley Online Library on [21/11/2022]. See the Terms and Conditions (https://onlinelibrary.wiley.com/terms-and-conditions) on Wiley Online Library for rules of use; OA articles are governed by the applicable Creative Commons License

Basin (Louca, Scranton, et al., 2019) and other similar marine anoxic zones (Chronopoulou et al., 2017; Hawley et al., 2014; Lam et al., 2009; Louca, Hawley, et al., 2016; Ulloa et al., 2012), including anaerobic ammonium oxidation to N_2 (anammox), oxidation of H_2S to SO_4^{2-} using NO_3^- (reduced to NO_2^-) or using NO_2^- (reduced to N_2), aerobic oxidation of H_2S to SO_4^{2-}, oxidation of H_2S to SO_4^{2-} via dissimilatory nitrate reduction to ammonium (DNRA), the two nitrification steps ($NH_4^+ \rightarrow NO_2^- \rightarrow NO_3^-$), and oxidation of methane using either O_2, NO_3^- (reduced to NO_2^-) or NO_2^- (reduced to N_2). To parameterize this model we only need the time- and depth-dependent vertical eddy diffusivity (Figure S3C, taken from Louca, Astor, et al., 2019), the boundary concentrations at the top and bottom of the considered depth interval, the reaction stoichiometries, and the initial concentration profiles in January 2001 (if brief transients are of interest), all of which would be required in conventional biogeochemical models as well; in contrast to conventional models, however, our FRT model does not require any knowledge of microbial species composition, population dynamics or reaction kinetics. The model also makes no assumption regarding proximity to steady state.

Despite its simplicity, the model predicts the spatiotemporal dynamics of dissolved O_2, NH_4^+, NO_3^-, H_2S and CH_4 concentrations during the years 2001–2014 and across the entire depth range to a remarkable accuracy. The Pearson correlation (r) between model predictions and data ranged from 0.90 to 0.99 depending on the substance, when evaluated uniformly across the entire spatiotemporal domain based on linear data interpolations (Figure 3), or from 0.81 to 0.97 when evaluated at the original data points (Figure S4). In particular, the model reproduces the general location of the redoxcline in this system over time, in response to seasonal oscillations of electron acceptor availability and decadal trends in H_2S input at the bottom. This demonstrates the computational tractability of the FRT approach and the accuracy that it can achieve in realistic situations. Further, these results show that microbially driven sulfur and nitrogen transformations in the considered depth range of the Cariaco Basin are largely consistent with the FRT limit and thus, in particular, diffusion limited and largely decoupled from the specific local microbial population dynamics and reaction kinetics. This suggests that observed decadal changes in sulfur dynamics in the Cariaco Basin water column are unlikely to be caused by concurrently observed shifts in the resident microbial communities; in fact, the causal relationship is more likely to be reversed, that is, shifts in community composition are potentially a result of shifting redox conditions, thus confirming previous interpretations (Taylor et al., 2012, 2018). The FRT model also yields insights that are hard to obtain with direct measurements, for example, regarding total denitrification rates and the precise locations at which each electron donor or acceptor is consumed. Indeed, the model reveals the formation of two reaction fronts separated by about 10 m, with methane oxidized in the deeper front, and H_2S and NH_4^+ mostly oxidized in the shallower front. Much of the activity of the modelled pathways is restricted to these reaction fronts, with negligible activity predicted at deeper sections (e.g., below 400 m). We emphasize that the locations of the reaction fronts are not particularly special in terms of the system's physical structure (e.g. no sharp pycnocline or thermocline occurs at those depths). Instead, the depth of these reaction fronts is largely determined by the stoichiometric balance of electron donor and acceptor fluxes across the water column, which in turn depends on boundary concentrations and vertical transport dynamics.

The predicted depth at which denitrification peaks (in terms of N_2 production), shown in Figure 3M, broadly resembles the depths at which most of the dark carbon assimilation (DCA) has previously been observed (Figure 3G), suggesting a close coupling between denitrification and DCA in this system. Lastly, the model can be used to test the relative importance of shifting boundary conditions compared to those of other environmental changes, such as variations in temperature or diffusivity. For example, when we re-ran the model with time-independent temperature and diffusivity profiles (at each depth set to the average value over time), the predicted metabolite concentrations remained nearly the same (Figure S5). This suggests that the dramatic changes in the system's redox conditions over time are largely driven by changes in the system's boundary conditions, most notably changes in the influx of methane and sulfide from the bottom (Figure 3K,L).

Caveats and open questions

The above results show that FRT models are computationally tractable and suitable for describing the biogeochemical trajectory of real microbial systems; however a number of caveats and questions remain. First, it should be made clear that the implementation of the FRT limit presented here is a priori only a numerical (i.e. algorithmic) one. Explicit differential/integral/algebraic equations that directly describe the dynamics of arbitrary microbial systems in the FRT limit (e.g. similar to the differential-algebraic systems obtained for abiotic ERT models) are unknown to us at this point, and it is not clear whether they can ever be found. Finding such explicit equations is a worthwhile goal, as they could yield additional valuable insight beyond what is accessible numerically and may even be useful for designing improved numerical routines for simulating FRT models.

Our results demonstrate that FRT models are capable of explaining and predicting the net fluxes and

14622920, 0, Downloaded from https://sfamjournals.onlinelibrary.wiley.com/doi/10.1111/1462-2920.16275 by University Of Oregon, Wiley Online Library on [21/11/2022]. See the Terms and Conditions (https://onlinelibrary.wiley.com/terms-and-conditions) on Wiley Online Library for rules of use; OA articles are governed by the applicable Creative Commons License

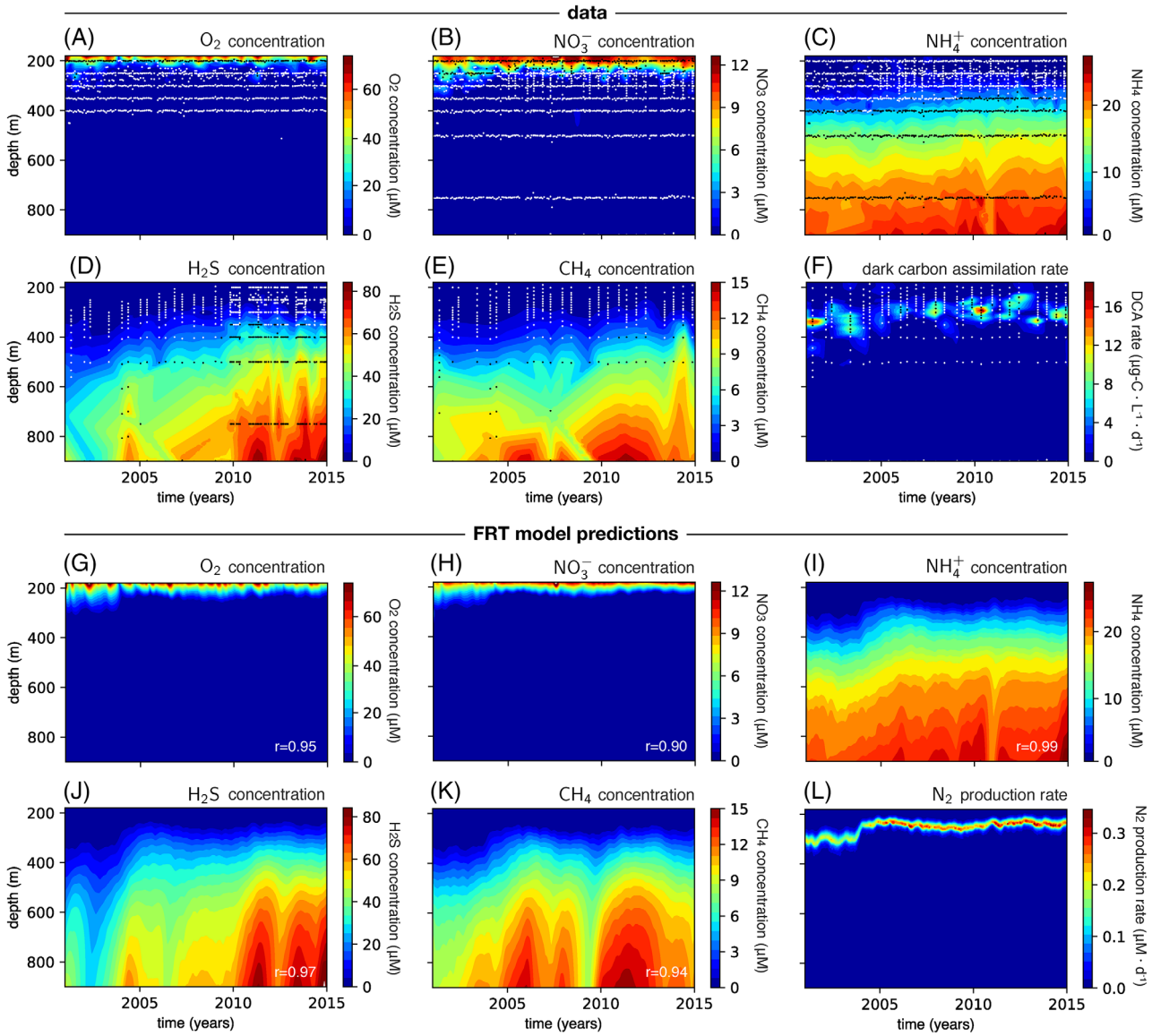

FIGURE 3 Cariaco Basin model versus data. (A–G) concentrations of dissolved oxygen (O_2), nitrate (NO_3^-), ammonium (NH_4^+), hydrogen sulfide (H_2S) and methane (CH_4), as well as dark carbon assimilation rates, measured across depth and time in the Cariaco Basin (Muller-Karger et al., 2019; Taylor et al., 2018). Black or white dots show the original data points, contours show interpolated values. (H–M) Concentrations of dissolved O_2, NO_3^-, NH_4^+, H_2S and CH_4, as well as rates of N_2 production (fixed nitrogen loss), predicted by the FRT model. In (H–L), the Pearson correlation between the model predictions and data (r) is shown in the figures (all were statistically significant, $p < 0.01$). For scatterplots, comparing model predictions to non-interpolated measurements, see Figure S4. For predicted net metabolite production/consumption rates across depth see Figure S6.

emerging distributions of various substrates and products of microbial metabolism, across space and time. Depending on the set of considered reactions, however, FRT models may not be suitable for reconstructing the rates of individual reactions. This is because many alternative combinations of reaction rates can lead to the same net outcome in terms of net chemical production/consumption rates. More specifically, various alternative trajectories during a fast reaction stage in a single grid cell could in principle lead to the same dead-end state. Conceptually, this is analogous to physical systems whose ground state may be computed based on first principles, but whose specific trajectory toward their ground state is much harder to predict (Franz et al., 2001; Likos, 2006). As an approximate rule, we generally expect that systems with a greater ratio of considered reactions over considered substances will tend to be more prone to this identifiability issue.

It should also be clear that, for systems in which mixing occurs at similar or shorter time scales than microbial population dynamics and metabolism, a pure FRT approach will unlikely be suitable. Such situations may be encountered for example in the mixed ocean

14622920, 0, Downloaded from https://sfamjournals.onlinelibrary.wiley.com/doi/10.1111/1462-2920.16275 by University Of Oregon, Wiley Online Library on [21/11/2022]. See the Terms and Conditions (https://onlinelibrary.wiley.com/terms-and-conditions) on Wiley Online Library for rules of use; OA articles are governed by the applicable Creative Commons License

layer, or in holomictic lakes during periods of intense mixing. In intermediate situations where mixing occurs predominantly during some brief periods separated by long periods of stratification, an FRT approach could be applied for the stratification periods, with simulations 'reset' appropriately after each fast mixing period. For example, such FRT models could be used to describe the gradual seasonal buildup of anoxic conditions and the resulting biogeochemical fluxes in some marine fjords with annual deep-water renewals, such as Saanich Inlet (Anderson & Devol, 1973; Manning et al., 2010), or in seasonally anoxic lakes (Hamilton-Taylor et al., 2005; Johnson et al., 1991).

CONCLUDING REMARKS

The presented FRT framework provides a substantially simplified approach to modelling abiotic as well as microbially catalyzed reactions and resulting chemical fluxes across space and time, in the frequently encountered scenario where reaction kinetics and underlying microbial population dynamics operate at much shorter time scales than physical transport and variations in boundary conditions. The benefits of the FRT approach are wide-ranging, because it eliminates the need for hard-to-obtain microbial physiological and kinetic parameters and knowledge of local microbial community composition. Indeed, FRT models could facilitate ecosystem/biogeochemical forecasts in systems for which the future composition of microbial communities (and their evolutionary response) is highly uncertain, for example, as part of climate models. Similarly, FRT models could also aid in paleoclimatic reconstructions, for example, by quantitatively linking boundary concentrations of nitrogen species to denitrification rates and thus isotopic ratios observed in sediments (Thunell et al., 2004). In contrast to existing ERT models (Goddard, 1990; Lichtner, 1985; Rubin, 1983), which can be seen as a special case of the FRT framework, the FRT framework can also accommodate non-reversibly catalyzed reactions and is thus applicable to a much wider range of biological scenarios.

Our results also have fundamental conceptual implications for interpreting the behaviour of complex biotic–abiotic systems, such as marine anoxic zones and sediments. Indeed, the activity of any transport-limited pathway, while strictly speaking biological in nature, may be largely forced by physical/chemical constraints, and biological complexities and uncertainties (while undoubtedly plenty) may only have a marginal net effect on a system's emergent biogeochemical dynamics. This situation is analogous to a classical result in differential equation theory, where the steady-state solution of the diffusion equation on a closed domain is entirely determined by the values on the domain's boundary (Linge & Langtangen, 2017), although the presence of reactions in FRT models will generally lead to markedly different dynamics than pure diffusion. We have presented evidence that the FRT limit applies to multiple important metabolic pathways in the Cariaco Basin redoxcline, a system whose microbiology has been the topic of intense investigations for decades (Hashimoto et al., 1983; Muller-Karger et al., 2019; Reeburgh, 1976). The FRT limit can thus help explain the decoupling between microbial taxonomic variation and function, frequently reported for marine and other aquatic systems (Coles et al., 2017; Louca et al., 2020; Louca, Parfrey, & Doebeli, 2016; Ramírez-Flandes et al., 2019). Comparison of data to FRT models can also help distinguish diffusion-limited from kinetically limited reactions and thus help prioritize costly efforts to determine kinetic parameters.

EXPERIMENTAL PROCEDURES

Sulfide oxidation example

The sulfide oxidation FRT model discussed in the main text, and summarized in Figure 2A–C, was constructed as follows. A single non-reversibly catalyzed reaction was assumed, representing aerobic sulfide oxidation:

$$H_2S + 2O_2 \rightarrow SO_4^{2-} + 2H^+, \quad \Delta G^o = -751.8\ \mathrm{kJ \cdot mol^{-1}}. \tag{3}$$

The concentration of H^+ was fixed at 2.4×10^{-8} M throughout, based on a pH of 7.62 typically encountered in the Cariaco redoxcline (Muller-Karger et al., 2019), and the concentration of SO_4^{2-} was fixed at 28 mM throughout based on typical seawater (Crowe et al., 2014). Hence, the model explicitly tracks only the concentrations of the electron donor H_2S and electron acceptor O_2. The vertical eddy diffusivity $\mathbb{D}$ was assumed to be equal to $170\,\mathrm{m}^2 \cdot \mathrm{d}^{-1}$, based on typical diffusivities estimated in the Cariaco redoxcline (Louca, Astor, et al., 2019). The temperature was set to 18°C (Muller-Karger et al., 2019), and advection was assumed to be zero. The concentration of O_2 was fixed at 160 μM at the top boundary and at 0 at the bottom boundary. The concentration of H_2S was fixed at 60 μM at the bottom boundary and at 0 at the top boundary, reflecting typical sulfide concentrations at the bottom of the Cariaco Basin (Louca, Astor, et al., 2019; Muller-Karger et al., 2019). The initial concentrations of O_2 and H_2S were set to 160 μM and zero, respectively. Depth was evenly discretized into 200 grid cells (spanning in total 1000 m), and the fast reaction stage was repeated every 2 days; further increasing the spatial resolution or the frequency of the fast reaction stage had negligible effects on the simulation outcome. Each transport stage thus covered 2 consecutive days and

14622920, 0, Downloaded from https://sfamjournals.onlinelibrary.wiley.com/doi/10.1111/1462-2920.16275 by University Of Oregon, Wiley Online Library on [21/11/2022]. See the Terms and Conditions (https://onlinelibrary.wiley.com/terms-and-conditions) on Wiley Online Library for rules of use; OA articles are governed by the applicable Creative Commons License

was integrated using MATLAB's `pdepe` partial differential equation solver. The standard Gibbs free energy of the reaction was calculated using the R package `CHNOSZ` v1.4.3 (Dick, 2019). During the fast reaction stage, a dead end was assumed to be reached once all reactions became non-endergonic ($\Delta G \geq 0$); however, we also tested alternative free energy thresholds ('biological energy quanta, ΔG^{m}, details in Supplement S.3) between 0 and $-20\,\mathrm{kJ} \cdot \mathrm{mol}^{-1}$ and found no noticeable differences in the model predictions (Pearson $r \geq 0.99$ when comparing predicted chemical concentrations). We emphasize that while parameters were largely based on the Cariaco Basin, this model was only meant to illustrate some typical dynamics expected in the FRT limit and was not intended for reproducing Cariaco's actual behaviour. Self-contained MATLAB code for simulating this example FRT model is available at www.loucalab.com/archive/FastReactionTransport.

Methane and sulfide oxidation example

The methane/sulfide oxidation FRT model discussed in the main text, and summarized in Figure 2D–I, was constructed as follows. The following two non-reversibly catalyzed reactions were assumed, representing sulfate-dependent anaerobic oxidation of methane and aerobic sulfide oxidation, respectively:

$$\begin{aligned} &H_2S + 2O_2 \rightarrow SO_4^{2-} + 2H^+, \quad \Delta G^o = -751.8\ \mathrm{kJ} \cdot \mathrm{mol}^{-1} \\ &CH_4 + SO_4^{2-} + 2H^+ \rightarrow CO_2 + H_2S + 2H_2O, \\ &\Delta G^o = -107.9\ \mathrm{kJ} \cdot \mathrm{mol}^{-1}. \end{aligned} \tag{4}$$

As in the previous example, the concentration of H^+ was fixed at 2.4×10^{-8} M, activity of H_2O was fixed at 1, and temperature was set to 18°C. The concentration of CO_2 was set to 0.027 μM (Muller-Karger et al., 2019) and the activity of H_2O was fixed at 1. Hence, the model explicitly tracks only the concentrations of the electron donors H_2S, CH_4 and electron acceptors O_2, SO_4^{2-}. The concentration of H_2S was fixed at zero at the top boundary and the flux of H_2S was fixed at zero at the bottom boundary. The concentration of CH_4 was fixed at zero at the top boundary and at 300 μM at the bottom boundary. The concentration of SO_4^{2-} was fixed at 300 μM at the top boundary and at zero at the bottom boundary. The time-dependent concentration of O_2 (in μM) at the top boundary was set to $160 \cdot [1 + 0.75 \cdot \sin(2\pi t)]$ (with t measured in years). The concentration of O_2 was fixed at zero at the bottom boundary. The initial concentrations were $[H_2S] = 0$, $[O_2] = 160\,\mu\mathrm{M}$, $[CH_4] = 300\,\mu\mathrm{M}$ and $\left[SO_4^{2-}\right] = 300\ \mu\mathrm{M}$. The vertical (molecular) diffusivity was set to $8.2 \times 10^{-5}\ \mathrm{m}^2 \cdot \mathrm{d}^{-1}$ for H_2S (Niewöhner et al., 1998; Roden & Tuttle, 1992), to $9.4 \times 10^{-5}\ \mathrm{m}^2 \cdot \mathrm{d}^{-1}$ for O_2 (Han & Bartels, 1996), to $4.8 \times 10^{-5}\ \mathrm{m}^2 \cdot \mathrm{d}^{-1}$ for SO_4^{2-} (Niewöhner et al., 1998) and to $7.5 \times 10^{-5}\ \mathrm{m}^2 \cdot \mathrm{d}^{-1}$ for CH_4 (Niewöhner et al., 1998). Depth was evenly discretized into 200 grid cells (spanning in total 20 cm), and the fast reaction stage was repeated every 0.2 days. Standard Gibbs free energies of reactions were calculated using the R package `CHNOSZ`. Similarly to the previous example, we found not noticeable effects of the assumed free energy threshold ($-20\,\mathrm{kJ} \cdot \mathrm{mol}^{-1} \leq \Delta G^{m} \leq 0$) on the model predictions (Pearson $r \geq 0.99$ when comparing predicted chemical concentrations). As for the previous example, we emphasize that this model was only meant to illustrate some typical dynamics expected in the FRT limit and was not intended for accurately reproducing the behaviour of a specific system. Self-contained MATLAB code for simulating this example FRT model is available at www.loucalab.com/archive/FastReactionTransport.

Nitrification and anammox example

To illustrate the effects that fast reaction reversibility can have on model predictions, we constructed two similar FRT models for nitrification and anammox in a water column (Figure S2), as follows. The following three fast reactions were assumed, representing the two nitrification steps and anammox, respectively:

$$\begin{aligned} &2NH_4^+ + 3O_2 \rightarrow 2H_2O + 2NO_2^- + 4H^+, \\ &\Delta G^o = -430.6\ \mathrm{kJ} \cdot \mathrm{mol}^{-1} \\ &2NO_2^- + O_2 \rightarrow 2NO_3^-, \quad \Delta G^o = -174.3\ \mathrm{kJ} \cdot \mathrm{mol}^{-1} \\ &NH_4^+ + NO_2^- \rightarrow N_2 + 2H_2O, \\ &\Delta G^o = -344.5\ \mathrm{kJ} \cdot \mathrm{mol}^{-1}. \end{aligned} \tag{5}$$

Similarly to the earlier sulfide oxidation example, we fixed the concentration of H^+ at 2.4×10^{-8} M and the activity of H_2O at 1. Hence, the models explicitly track the concentrations of NH_4^+, NO_3^-, NO_2^-, N_2 and O_2. As in the sulfide oxidation example, the vertical eddy diffusivity $\mathbb{D}$ was fixed at $170\,\mathrm{m}^2 \cdot \mathrm{d}^{-1}$, the temperature was set to 18°C, and advection was assumed to be zero. The concentration of O_2 was fixed at 100 μM at the top boundary and at 0 at the bottom boundary. The concentration of NH_4^+ was fixed at 100 μM at the bottom boundary and at 0 at the top boundary. The concentrations of NO_3^- and NO_2^- were fixed at zero at both boundaries. The concentration of N_2 was fixed at 600 μM at the top boundary based on typical concentrations in the ocean (Craig et al., 1967), and the flux of N_2 was set to 0 at the bottom boundary. The initial concentrations of NH_4^+, NO_3^-, NO_2^- and O_2 were set to zero, while the initial concentration of N_2 was set to 600 μM.

14622920, 0, Downloaded from https://sfamjournals.onlinelibrary.wiley.com/doi/10.1111/1462-2920.16275 by University Of Oregon, Wiley Online Library on [21/11/2022]. See the Terms and Conditions (https://onlinelibrary.wiley.com/terms-and-conditions) on Wiley Online Library for rules of use; OA articles are governed by the applicable Creative Commons License

Depth was evenly discretized into 200 grid cells (spanning in total 1000 m), and the fast reaction stage was repeated every 2 days. Standard Gibbs free energies of reactions were calculated using the R package CHNOSZ. We either assumed that all reactions were non-reversibly catalyzed (Model 1) or reversible (Model 2). Model 1 was simulated similarly to the previous two examples, while Model 2 was simulated by solving for local equilibrium at each fast reaction stage (i.e. determining $\mathbf{H} \in \mathbb{R}^3$ such that $\widetilde{\mathbf{C}}(0) + \mathbb{S} \cdot \mathbf{H}$ is a thermodynamic equilibrium state in each spatial grid cell) using the MATLAB function fsolve.

Cariaco Basin data

Data were downloaded from the CARIACO Ocean Time Series project website (http://www.imars.usf.edu/cariaco) on 28 April 2018. Methods of data collection were described previously (Muller-Karger et al., 2019; Scranton et al., 2014). Some of the hydrogen sulfide concentration data, published by Muller-Karger et al. (2019), were obtained directly from the authors. To determine the chemical boundary concentrations at the top and bottom and to compare model predictions to data, chemical concentration data were bilinearly interpolated on a regular spatiotemporal grid (Figure 3A–F). Previously estimated vertical eddy diffusivities were obtained from (Louca, Astor, et al., 2019). Temperature, salinity and diffusivity are shown in Figure S3.

Cariaco Basin model

The Cariaco Basin FRT model considers the following non-reversibly biologically catalyzed reactions:

$$2NH_4^+ + 3O_2 \rightarrow 2H_2O + 2NO_2 + 4H^+, \quad \Delta G^o = -430.6\ \mathrm{kJ \cdot mol^{-1}} \tag{6}$$

$$2NO_2^- + O_2 \rightarrow 2NO_3^-, \quad \Delta G^o = -174.3\ \mathrm{kJ \cdot mol^{-1}} \tag{7}$$

$$NH_4^+ + NO_2^- \rightarrow N_2 + 2H_2O, \quad \Delta G^o = -344.5\ \mathrm{kJ \cdot mol^{-1}} \tag{8}$$

$$H_2S + 2O_2 \rightarrow SO_4^{2-} + 2H^+, \quad \Delta G^o = -751.8\ \mathrm{kJ \cdot mol^{-1}} \tag{9}$$

$$H_2S + 4NO_3^- \rightarrow 4NO_2 + SO_4^{2-} + 2H^+, \quad \Delta G^o = -403.2\ \mathrm{kJ \cdot mol^{-1}} \tag{10}$$

$$3H_2S + 8NO_2^- + 2H^+ \rightarrow 4N_2 + 3SO_4^{2-} + 4H_2O, \quad \Delta G^o = -2772.4\ \mathrm{kJ \cdot mol^{-1}} \tag{11}$$

$$H_2S + NO_3^- + H_2O \rightarrow NH_4^+ + SO_4^{2-}, \quad \Delta G^o = -449.4\ \mathrm{kJ \cdot mol^{-1}} \tag{12}$$

$$CH_4 + 2O_2 \rightarrow CO_2 + 2H_2O, \quad \Delta G^o = -859.7\ \mathrm{kJ \cdot mol^{-1}} \tag{13}$$

$$CH_4 + 4NO_3^- \rightarrow CO_2 + 4NO_2^- + 2H_2O, \quad \Delta G^o = -511.0\ \mathrm{kJ \cdot mol^{-1}} \tag{14}$$

$$3CH_4 + 8NO_2^- + 8H^+ \rightarrow 3CO_2 + 4N_2 + 10H_2O, \quad \Delta G^o = -3096.0\ \mathrm{kJ \cdot mol^{-1}} \tag{15}$$

Sulfate-dependent anaerobic methane oxidation was not included because no strong evidence exists so far that it occurs to substantial amounts in marine water columns; the fact that SO_4^{2-} and CH_4 overlap substantially across several hundreds of meters of depth in the Cariaco Basin water column (Donahue et al., 2008; Kessler et al., 2006), and the fact that our FRT model closely reproduces the observed methane profiles, suggests that this reaction, if it occurs, must be severely kinetically limited in the water column. Alternatively, sulfate-driven methane oxidation might in principle occur in the water column as part of a cryptic cycle inside particles, where methane oxidation is matched by in situ methanogenesis; such a cryptic small-scale cycle, however, cannot be resolved by an FRT model (see Caveats and open questions section). Organic carbon remineralization was omitted from the model for two reasons: first, within the considered depth range, chemolithoautotrophy rates are thought to dominate over heterotrophy rates (Taylor et al., 2018) (also see

14622920, 0, Downloaded from https://sfamjournals.onlinelibrary.wiley.com/doi/10.1111/1462-2920.16275 by University Of Oregon, Wiley Online Library on [21/11/2022]. See the Terms and Conditions (https://onlinelibrary.wiley.com/terms-and-conditions) on Wiley Online Library for rules of use; OA articles are governed by the applicable Creative Commons License

Figure 3G and Figure S7) and to be mostly fuelled by upward diffusing inorganic electron donors and downward diffusing electron acceptors (Li et al., 2012; Taylor et al., 2018). Second, organic carbon remineralization is a complex process that involves multiple steps, some of which are likely kinetically limited. For example, extracellular enzymatic hydrolysis, an important and often rate-limiting early step in organic carbon remineralization (Chróst, 1990), may be kinetically limited by the efficiency of hydrolytic enzymes and their ability to access organic matter particles (Rothman & Forney, 2007). An inclusion of these processes would have substantially complicated our model. The fact that our model largely captured the major dynamics of considered metabolites suggests that organic carbon remineralization only has a minor effect on these dynamics, thus confirming (in retrospect) our model's adequacy.

Lateral transport was assumed to be much faster than vertical transport, thus leading to a laterally homogeneous model with a single spatial axis corresponding to depth, similarly to previous models of this system (Li et al., 2012; Louca, Astor, et al., 2019; Louca, Scranton, et al., 2019; Scranton et al., 1987). Vertical transport of dissolved metabolites was assumed to be largely via eddy (turbulent) diffusion; hence, the advection speed was set to zero. The depth- and time-dependent diffusivity was taken from Louca, Astor, et al. (2019). Depth was discretized into 200 evenly sized grid cells, spanning 180–900 m, and the fast reaction stage was repeated every 5 days; further increasing the spatial resolution or increasing the frequency of the fast reaction stage had negligible effects on the simulation outcomes. The model accounts for geometric dilution effects due to variation of the basin's lateral (cross section) area with depth, using an appropriately modified diffusion–advection equation and lateral area estimates by Samodurov et al. (2013), as described previously (Louca, Scranton, et al., 2019, SI Appendix S.3). Briefly, this can be done by replacing the transport term on the right side of Equation (1) with the following expression:

$$\frac{\partial}{\partial z}\left(\mathbb{D}_m \frac{\partial C_m}{\partial z} - \mathrm{v}_m C_m\right) + \frac{1}{w}\frac{\partial w}{\partial z}\cdot\left(\mathbb{D}_m \frac{\partial C_m}{\partial z} - \mathrm{v}_m C_m\right), \tag{16}$$

where z denotes depth, $\mathbb{D}_m$ is the vertical diffusivity, v_m is the vertical advection speed (which is 0 in our case), and $w(z)$ is the lateral (cross section) area of the basin at depth z. The concentration of H^+ was fixed at 0.024 μM based on a typical pH of 7.62 in Cariaco Basin, and the activity of H_2O was fixed at 1; all other metabolites involved in the modelled reactions were explicitly tracked. For each time point, boundary concentrations were taken from the chemical concentration time series at the top (180 m) and bottom (900 m) boundaries, except in the following cases: $[H_2S]$ and $[NH_4^+]$ at the top were fixed at 0, while $[O_2]$ and $[NO_3^-]$ at the bottom were fixed at 0. The initial concentrations of explicitly tracked metabolites in January 2001 (only needed if early transients are of interest) were determined from the available data via bilinear interpolation. Standard Gibbs free energies of reactions were calculated using the R package `CHNOSZ`, at atmospheric pressure. In the fast reaction stage, a dead end was assumed to be reached once all reactions became non-endergonic ($\Delta G \geq 0$). However, when we considered alternative free energy thresholds ($-20\,\mathrm{kJ}\cdot\mathrm{mol}^{-1} \leq \Delta G^m \leq 0$), the effects on predicted metabolite concentrations were negligible for almost all metabolites (Pearson $r \geq 0.99$) except for NO_2^-, which was always predicted to be essentially absent ($[NO_2^-] \ll 1$ nM). Self-contained MATLAB code for simulating this example FRT model is available at www.loucalab.com/archive/FastReactionTransport.

AUTHOR CONTRIBUTIONS

Stilianos Louca conceived the project and performed the mathematical and computational analyses. All authors contributed to the writing of the manuscript. Gordon T. Taylor, Yrene M. Astor, Kristen N. Buck and Frank E. Muller-Karger were instrumental in the CARIACO Time Series program.

ACKNOWLEDGEMENTS

Stilianos Louca was supported by an Alfred P. Sloan fellowship and by a Simons Foundation early career investigator award. Gordon T. Taylor was supported by NSF grants OCE-9415790, 9711318, 9730278, 0118491, 0326175, 0752014, and 1259110. The authors are thankful to the scientific personnel of the Fundación La Salle de Ciencias Naturales de Venezuela (FLASA), the Estación de Investigaciones Marinas de Margarita (FLASA/EDIMAR), and the crew of the R/V Hermano Ginés (FLASA). The authors also thank the numerous students, technicians, scientific support staff, researchers and professors that contributed to the CARIACO time-series program. The project was supported financially by the Consejo Nacional de Ciencia y Tecnología (96280221), the Fondo Nacional de Ciencia, Tecnología e Investigación (2000001702 and 2011000353), and the Ley de Ciencia, Tecnología e Innovación (Estación de Investigaciones Marinas, 23914) in Venezuela; the National Science Foundation (OCE-0752139, OCE-9216626, OCE-9729284, OCE-491 9401537, OCE-9729697, OCE-9415790, OCE-9711318, OCE-0326268, OCE-0963028, OCE-0326313) and NASA (NAG5-6448, NAS5-97128, and NNX14AP62A) in the United States; and the Inter-American Institute for Global Change Research (IAI-CRN3094). The authors thank Nathan Malamud for exploratory analyses that motivated this project.

14622920, 0, Downloaded from https://sfamjournals.onlinelibrary.wiley.com/doi/10.1111/1462-2920.16275 by University Of Oregon, Wiley Online Library on [21/11/2022]. See the Terms and Conditions (https://onlinelibrary.wiley.com/terms-and-conditions) on Wiley Online Library for rules of use; OA articles are governed by the applicable Creative Commons License

CONFLICT OF INTEREST

The authors declare no conflict of interest.

DATA AVAILABILITY STATEMENT

Data used in this article are publicly available at the Cariaco Basin Time Series project website (imars.usf.edu/cariaco). The data are also available at the US Biological and Chemical Oceanography Data Management Office (BCO-DMO, www.bco-dmo.org/project/2047), where the following collections can be found: Hydrographic parameters (DOI: 10.1575/1912/bco-dmo.3093.1), biogeochemistry and microbiology (DOI:10.1575/1912/bco-dmo.3120.1), HPLC (DOI: 10.1575/1912/bco-dmo.3293.1, DOI: 10.1575/1912/bco-dmo.3235.1, DOI: 10.1575/1912/bco-dmo.3292.1, DOI:10.1575/1912/bco-dmo.777689.1), CTD profiles (DOI:10.1575/1912/bco-dmo.3092.1, DOI:10.1575/1912/bco-dmo.773146.1). Alternative sources of CARIACO time series data are the NOAA National Centers for Environmental Information (NCEI, accessions 0191401, 0189595, 0201747), the Ocean Carbon Data System and the NASA SeaBASS database.

REFERENCES

Alberty, R.A. & Hammes, G.G. (1958) Application of the theory of diffusion-controlled reactions to enzyme kinetics. *The Journal of Physical Chemistry*, 62, 154–159.

Anderson, J.J. & Devol, A.H. (1973) Deep water renewal in Saanich Inlet, an intermittently anoxic basin. *Estuarine and Coastal Marine Science*, 1, 1–10.

Aumont, O., Ethé, C., Tagliabue, A., Bopp, L. & Gehlen, M. (2015) PISCES-v2: an ocean biogeochemical model for carbon and ecosystem studies. *Geoscientific Model Development*, 8, 2465–2513.

Boudreau, B.P. (1991) Modelling the sulfide-oxygen reaction and associated pH gradients in porewaters. *Geochimica et Cosmochimica Acta*, 55, 145–159.

Brettar, I. & Rheinheimer, G. (1991) Denitrification in the Central Baltic: evidence for H_2S-oxidation as motor of denitrification at the oxic-anoxic interface. *Marine Ecology Progress Series*, 77, 157–169.

Canfield, D.E. & Thamdrup, B. (2009) Towards a consistent classification scheme for geochemical environments, or, why we wish the term 'suboxic' would go away. *Geobiology*, 7, 385–392.

Carstensen, J., Andersen, J.H., Gustafsson, B.G. & Conley, D.J. (2014) Deoxygenation of the Baltic Sea during the last century. *Proceedings of the National Academy of Sciences*, 111, 5628–5633.

Chronopoulou, P.M., Shelley, F., Pritchard, W.J., Maanoja, S.T. & Trimmer, M. (2017) Origin and fate of methane in the Eastern Tropical North Pacific oxygen minimum zone. *The ISME Journal*, 11, 1386–1399.

Chróst, R.J. (1990) Microbial ectoenzymes in aquatic environments. In: Overbeck, J. & Chróst, R.J. (Eds.) *Aquatic microbial ecology: biochemical and molecular approaches*. New York, NY: Springer, pp. 47–78.

Coles, V.J. & Hood, R.R. (2016) *Approaches and challenges for linking marine biogeochemical models with the "omics" revolution*. Switzerland: Springer International Publishing, pp. 45–63.

Coles, V.J., Stukel, M.R., Brooks, M.T., Burd, A., Crump, B.C., Moran, M.A. et al. (2017) Ocean biogeochemistry modeled with emergent trait-based genomics. *Science*, 358, 1149–1154.

Craig, H., Weiss, R. & Clarke, W. (1967) Dissolved gases in the equatorial and South Pacific Ocean. *Journal of Geophysical Research*, 72, 6165–6181.

Crowe, S.A., Paris, G., Katsev, S., Jones, C., Kim, S.T., Zerkle, A.L. et al. (2014) Sulfate was a trace constituent of Archean seawater. *Science*, 346, 735–739.

Debnath, T., Ghosh, P.K., Li, Y., Marchesoni, F. & Nori, F. (2019) Active diffusion limited reactions. *The Journal of Chemical Physics*, 150, 154902.

Deutzmann, J.S. (2020) Anaerobic methane oxidation in freshwater environments. In: Boll, M. (Ed.) *Anaerobic utilization of hydrocarbons, oils, and lipids*. Cham, Switzerland: Springer, pp. 391–404.

Diaz, R.J. & Rosenberg, R. (2008) Spreading dead zones and consequences for marine ecosystems. *Science*, 321, 926–929.

Dick, J.M. (2019) CHNOSZ: thermodynamic calculations and diagrams for geochemistry. *Frontiers in Earth Science*, 7, 180.

Donahue, M.A., Werne, J.P., Meile, C. & Lyons, T.W. (2008) Modeling sulfur isotope fractionation and differential diffusion during sulfate reduction in sediments of the Cariaco Basin. *Geochimica et Cosmochimica Acta*, 72, 2287–2297.

Franz, A., Hoffmann, K.H. & Salamon, P. (2001) Best possible strategy for finding ground states. *Physical Review Letters*, 86, 5219–5222.

Gibson, B., Wilson, D.J., Feil, E. & Eyre-Walker, A. (2018) The distribution of bacterial doubling times in the wild. *Proceedings of the Royal Society of London B: Biological Sciences*, 285, 20180789.

Gies, E.A. (2015) *Illuminating phylogeny and function of microbial dark matter in Sakinaw Lake*. Ph.D. thesis. Vancouver, BC, Canada: University of British Columbia.

Goddard, J.D. (1990) Consequences of the partial-equilibrium approximation for chemical reaction and transport. *Proceedings of the Royal Society A*, 431, 271–284.

Grote, J., Jost, G., Labrenz, M., Herndl, G.J. & Jürgens, K. (2008) Epsilonproteobacteria represent the major portion of chemoautotrophic bacteria in sulfidic waters of pelagic redoxclines of the Baltic and black seas. *Applied and Environmental Microbiology*, 74, 7546–7551.

Hamilton-Taylor, J., Smith, E.J., Davison, W. & Sugiyama, M. (2005) Resolving and modeling the effects of Fe and Mn redox cycling on trace metal behavior in a seasonally anoxic lake. *Geochimica et Cosmochimica Acta*, 69, 1947–1960.

Han, P. & Bartels, D.M. (1996) Temperature dependence of oxygen diffusion in H2O and D2O. *The Journal of Physical Chemistry*, 100, 5597–5602.

Hannig, M., Lavik, G., Kuypers, M., Woebken, D., Martens-Habbena, W. & Jürgens, K. (2007) Shift from denitrification to anammox after inflow events in the Central Baltic Sea. *Limnology and Oceanography*, 52, 1336–1345.

Hashimoto, L.K., Kaplan, W.A., Wofsy, S.C. & McElroy, M.B. (1983) Transformations of fixed nitrogen and N2O in the Cariaco trench. *Deep Sea Research Part A. Oceanographic Research Papers*, 30, 575–590.

Hawley, A.K., Brewer, H.M., Norbeck, A.D., Paša-Tolić, L. & Hallam, S.J. (2014) Metaproteomics reveals differential modes of metabolic coupling among ubiquitous oxygen minimum zone microbes. *Proceedings of the National Academy of Sciences*, 111, 11395–11400.

Hoehler, T.M. (2004) Biological energy requirements as quantitative boundary conditions for life in the subsurface. *Geobiology*, 2, 205–215.

Hordijk, K.A., Hagenaars, C.P.M.M. & Cappenberg, T.E. (1985) Kinetic studies of bacterial sulfate reduction in freshwater sediments by high-pressure liquid chromatography and microdistillation. *Applied and Environmental Microbiology*, 49, 434–440.

İnceoğlu, O., Llirós, M., Crowe, S.A., García-Armisen, T., Morana, C., Darchambeau, F. et al. (2015) Vertical distribution of functional

14622920, 0, Downloaded from https://sfamjournals.onlinelibrary.wiley.com/doi/10.1111/1462-2920.16275 by University Of Oregon, Wiley Online Library on [21/11/2022]. See the Terms and Conditions (https://onlinelibrary.wiley.com/terms-and-conditions) on Wiley Online Library for rules of use; OA articles are governed by the applicable Creative Commons License

potential and active microbial communities in meromictic Lake Kivu. *Microbial Ecology*, 70, 596–611.

Indrebo, G., Pengerud, B. & Dundas, I. (1979) Microbial activities in a permanently stratified estuary. II. Microbial activities at the oxic-anoxic interface. *Marine Biology*, 51, 305–309.

Iversen, N. & Jorgensen, B.B. (1985) Anaerobic methane oxidation rates at the sulfate-methane transition in marine sediments from Kattegat and Skagerrak (Denmark). *Limnology and Oceanography*, 30, 944–955.

Jackson, B.E. & McInerney, M.J. (2002) Anaerobic microbial metabolism can proceed close to thermodynamic limits. *Nature*, 415, 454–456.

Jin, Q. & Bethke, C.M. (2007) The thermodynamics and kinetics of microbial metabolism. *American Journal of Science*, 307, 643–677.

Johnson, C.A., Ulrich, M., Sigg, L. & Imboden, D.M. (1991) A mathematical model of the manganese cycle in a seasonally anoxic lake. *Limnology and Oceanography*, 36, 1415–1426.

Kartal, B., van Niftrik, L., Keltjens, J.T., Op den Camp, H.J. & Jetten, M. S. (2012) Anammox–growth physiology, cell biology, and metabolism. *Advances in microbial physiology*, 60, 211–262.

Kessler, J.D., Reeburgh, W.S. & Tyler, S.C. (2006) Controls on methane concentration and stable isotope ($\delta^2H - CH_4$ and $\delta^{13}C - CH_4$) distributions in the water columns of the Black Sea and Cariaco Basin. *Global Biogeochemical Cycles*, 20, GB4004.

Lam, P., Jensen, M.M., Lavik, G., McGinnis, D.F., Müller, B., Schubert, C.J. et al. (2007) Linking crenarchaeal and bacterial nitrification to anammox in the Black Sea. *Proceedings of the National Academy of Sciences*, 104, 7104–7109.

Lam, P., Lavik, G., Jensen, M.M., van de Vossenberg, J., Schmid, M., Woebken, D. et al. (2009) Revising the nitrogen cycle in the Peruvian oxygen minimum zone. *Proceedings of the National Academy of Sciences*, 106, 4752–4757.

Lehours, A.C., Bardot, C., Thenot, A., Debroas, D. & Fonty, G. (2005) Anaerobic microbial communities in Lake Pavin, a unique meromictic lake in France. *Applied and Environmental Microbiology*, 71, 7389–7400.

Li, X.N., Taylor, G.T., Astor, Y., Varela, R. & Scranton, M.I. (2012) The conundrum between chemoautotrophic production and reductant and oxidant supply: a case study from the Cariaco Basin. *Deep Sea Research Part I: Oceanographic Research Papers*, 61, 1–10.

Lichtner, P.C. (1985) Continuum model for simultaneous chemical reactions and mass transport in hydrothermal systems. *Geochimica et Cosmochimica Acta*, 49, 779–800.

Likos, C.N. (2006) Going to ground. *Nature*, 440, 433–434.

Linge, S. & Langtangen, H.P. (2017) *Diffusion Equations*. Cham, Switzerland: Springer International Publishing, pp. 207–322.

Louca, S., Astor, Y.M., Doebeli, M., Taylor, G.T. & Scranton, M.I. (2019) Microbial metabolite fluxes in a model marine anoxic ecosystem. *Geobiology*, 17, 628–642.

Louca, S., Hawley, A.K., Katsev, S., Torres-Beltran, M., Bhatia, M.P., Kheirandish, S. et al. (2016) Integrating biogeochemistry with multiomic sequence information in a model oxygen minimum zone. *Proceedings of the National Academy of Sciences*, 113, E5925–E5933.

Louca, S., Parfrey, L.W. & Doebeli, M. (2016) Decoupling function and taxonomy in the global ocean microbiome. *Science*, 353, 1272–1277.

Louca, S., Rubin, I.N., Bohlmann, J., Madilao, L.L., Doebeli, M. & Parfrey, L.W. (2020) Effects of forced taxonomic transitions on metabolic structure and function in microbial microcosms. *Environmental Microbiology Reports*, 12, 514–524.

Louca, S., Scranton, M.I., Taylor, G.T., Astor, Y.M., Crowe, S.A. & Doebeli, M. (2019) Circumventing kinetics in biogeochemical modeling. *Proceedings of the National Academy of Sciences*, 116, 11329–11338.

Manning, C.C., Hamme, R.C. & Bourbonnais, A. (2010) Impact of deep-water renewal events on fixed nitrogen loss from seasonally-anoxic Saanich inlet. *Marine Chemistry*, 122, 1–10.

Mostovaya, A., Wind-Hansen, M., Rousteau, P., Bristow, L.A. & Thamdrup, B. (2022) Sulfate- and iron-dependent anaerobic methane oxidation occurring side-by-side in freshwater lake sediment. *Limnology and Oceanography*, 67, 231–246.

Muller-Karger, F.E., Astor, Y.M., Benitez-Nelson, C.R., Buck, K.N., Fanning, K.A., Lorenzoni, L. et al. (2019) The scientific legacy of the CARIACO Ocean time-series program. *Annual Review of Marine Science*, 11, 5.1–5.25.

Murray, J.W., Jannasch, H.W., Honjo, S., Anderson, R.F., Reeburgh, W.S., Top, Z. et al. (1989) Unexpected changes in the oxic/anoxic interface in the Black Sea. *Nature*, 338, 411–413.

Neretnieks, I. (1993) Diffusion, flow and fast reactions in porous media. In: Petruzzelli, D. & Helfferich, F.G. (Eds.) *Migration and fate of pollutants in soils and subsoils*. Berlin, Heidelberg: Springer, pp. 329–354.

Niewöhner, C., Hensen, C., Kasten, S., Zabel, M. & Schulz, H.D. (1998) Deep sulfate reduction completely mediated by anaerobic methane oxidation in sediments of the upwelling area off Namibia. *Geochimica et Cosmochimica Acta*, 62, 455–464.

Oguz, T., Ducklow, H.W. & Malanotte-Rizzoli, P. (2000) Modeling distinct vertical biogeochemical structure of the black sea: dynamical coupling of the oxic, suboxic, and anoxic layers. *Global Biogeochemical Cycles*, 14, 1331–1352.

Preheim, S.P., Olesen, S.W., Spencer, S.J., Materna, A., Varadharajan, C., Blackburn, M. et al. (2016) Surveys, simulation and single-cell assays relate function and phylogeny in a lake ecosystem. *Nature Microbiology*, 1, 16130.

Ramírez-Flandes, S., González, B. & Ulloa, O. (2019) Redox traits characterize the organization of global microbial communities. *Proceedings of the National Academy of Sciences*, 116, 3630–3635.

Rasilainen, K., Luukkonen, A., Niemi, A., Olin, M. & Polla, J. (1999) *The feasibility of modelling coupled processes in safety analysis of spent nuclear fuel disposal, Technical Report VTT-TIED-1973*. Espoo, Finland: Technical Research Centre of Finland.

Reeburgh, W.S. (1976) Methane consumption in Cariaco Trench waters and sediments. *Earth and Planetary Science Letters*, 28, 337–344.

Reed, D.C., Algar, C.K., Huber, J.A. & Dick, G.J. (2014) Gene-centric approach to integrating environmental genomics and biogeochemical models. *Proceedings of the National Academy of Sciences*, 111, 1879–1884.

Resendis-Antonio, O. (2013) Stoichiometric matrix. In: Dubitzky, W., Wolkenhauer, O., Cho, K.H. & Yokota, H. (Eds.) *Encyclopedia of systems biology*. New York, NY: Springer, p. 2014.

Roden, E.E. & Tuttle, J.H. (1992) Sulfide release from estuarine sediments underlying anoxic bottom water. *Limnology and Oceanography*, 37, 725–738.

Roque, B. & Petroff, A. (2022) Oxygen dynamics in a vertically stratified microbial community. In: *APS March meeting 2022*. Chicago: American Physical Society.

Rothman, D.H. & Forney, D.C. (2007) Physical model for the decay and preservation of marine organic carbon. *Science*, 316, 1325–1328.

Rubin, J. (1983) Transport of reacting solutes in porous media: relation between mathematical nature of problem formulation and chemical nature of reactions. *Water Resources Research*, 19, 1231–1252.

Samodurov, A.S., Scranton, M.I., Astor, Y., Ivanov, L.I., Chukharev, A.M., Belokopytov, V.N. et al. (2013) Modeling vertical exchange of heat, salt, and other dissolved substances in the Cariaco Basin. *Deep Sea Research Part I: Oceanographic Research Papers*, 71, 61–72.

14622920, 0, Downloaded from https://sfamjournals.onlinelibrary.wiley.com/doi/10.1111/1462-2920.16275 by University Of Oregon, Wiley Online Library on [21/11/2022]. See the Terms and Conditions (https://onlinelibrary.wiley.com/terms-and-conditions) on Wiley Online Library for rules of use; OA articles are governed by the applicable Creative Commons License

Schink, B. (1997) Energetics of syntrophic cooperation in methanogenic degradation. *Microbiology and Molecular Biology Reviews*, 61, 262–280.

Scranton, M.I., Sayles, F.L., Bacon, M.P. & Brewer, P.G. (1987) Temporal changes in the hydrography and chemistry of the Cariaco Trench. *Deep Sea Research Part A. Oceanographic Research Papers*, 34, 945–963.

Scranton, M.I., Taylor, G.T., Thunell, R., Benitez-Nelson, C.R., Muller-Karger, F., Fanning, K. et al. (2014) Interannual and sub-decadal variability in the nutrient geochemistry of the Cariaco Basin. *Oceanography*, 27, 148–159.

Sonne-Hansen, J., Westermann, P. & Ahring, B.K. (1999) Kinetics of sulfate and hydrogen uptake by the thermophilic sulfate-reducing bacteria *Thermodesulfobacterium* sp. strain JSP and *Thermodesulfovibrio* sp. strain R1Ha3. *Applied and Environmental Microbiology*, 65, 1304–1307.

Sonthiphand, P., Hall, M.W. & Neufeld, J.D. (2014) Biogeography of anaerobic ammonia-oxidizing (anammox) bacteria. *Frontiers in Microbiology*, 5, 399.

Sorokin, D.Y., Foti, M., Pinkart, H.C. & Muyzer, G. (2007) Sulfur-oxidizing bacteria in Soap Lake (Washington State), a meromictic, haloalkaline lake with an unprecedented high sulfide content. *Applied and Environmental Microbiology*, 73, 451–455.

Stewart, P.S. & Franklin, M.J. (2008) Physiological heterogeneity in biofilms. *Nature Reviews Microbiology*, 6, 199.

Taylor, G.T., Iabichella, M., Ho, T.Y., Scranton, M.I., Thunell, R.C., Muller-Karger, F. et al. (2001) Chemoautotrophy in the redox transition zone of the Cariaco Basin: a significant midwater source of organic carbon production. *Limnology and Oceanography*, 46, 148–163.

Taylor, G.T., Muller-Karger, F., Thunell, R.C., Scranton, M., Astor, Y., Varela, R. et al. (2012) Ecosystem response to global climate change in the southern Caribbean Sea. *Proceedings of the National Academy of Sciences*, 109, 19–315.

Taylor, G.T., Suter, E.A., Pachiadaki, M.G., Astor, Y., Edgcomb, V. P. & Scranton, M.I. (2018) Temporal shifts in dominant sulfur-oxidizing chemoautotrophic populations across the Cariaco Basin's redoxcline. *Deep Sea Research Part II: Topical Studies in Oceanography*, 156, 80–96.

Thunell, R.C., Sigman, D.M., Muller-Karger, F., Astor, Y. & Varela, R. (2004) Nitrogen isotope dynamics of the Cariaco Basin, Venezuela. *Global Biogeochemical Cycles*, 18, GB3001.

Tilman, D. (1982) *Resource competition and community structure*. Princeton, NJ: Princeton University Press.

Treude, T., Niggemann, J., Kallmeyer, J., Wintersteller, P., Schubert, C.J., Boetius, A. et al. (2005) Anaerobic oxidation of methane and sulfate reduction along the Chilean continental margin. *Geochimica et Cosmochimica Acta*, 69, 2767–2779.

Ulloa, O., Canfield, D.E., DeLong, E.F., Letelier, R.M. & Stewart, F.J. (2012) Microbial oceanography of anoxic oxygen minimum zones. *Proceedings of the National Academy of Sciences*, 109, 15996–16003.

van Bodegom, P.M. & Scholten, J.C.M. (2001) Microbial processes of CH_4 production in a rice paddy soil: model and experimental validation. *Geochimica et Cosmochimica Acta*, 65, 2055–2066.

Vichi, M., Lovato, T., Butenschön, M., Tedesco, L., Lazzari, P., Cossarini, G. et al. (2020) *The biogeochemical flux model (BFM): equation description and user manual*. Bologna, Italy: Biogeochemical Flux Model consortium.

Wenk, C.B., Blees, J., Zopfi, J., Veronesi, M., Bourbonnais, A., Schubert, C.J. et al. (2013) Anaerobic ammonium oxidation (anammox) bacteria and sulfide-dependent denitrifiers coexist in the water column of a meromictic south-alpine lake. *Limnology and Oceanography*, 58, 1–12.

Wright, J.J., Konwar, K.M. & Hallam, S.J. (2012) Microbial ecology of expanding oxygen minimum zones. *Nature Reviews Microbiology*, 10, 381–394.

Yakushev, E.V. (2013) RedOx layer model: a tool for analysis of the water column oxic/anoxic interface processes. In: *The handbook of environmental chemistry*, Vol. 22. Berlin, Heidelberg: Springer, pp. 203–233.

Zaikova, E., Walsh, D.A., Stilwell, C.P., Mohn, W.W., Tortell, P.D. & Hallam, S.J. (2010) Microbial community dynamics in a seasonally anoxic fjord: Saanich Inlet, British Columbia. *Environmental Microbiology*, 12, 172–191.

Zhang, F., Yeh, G.T., Parker, J.C., Brooks, S.C., Pace, M.N., Kim, Y. J. et al. (2007) A reaction-based paradigm to model reactive chemical transport in groundwater with general kinetic and equilibrium reactions. *Journal of Contaminant Hydrology*, 92, 10–32.

Zubkov, M., Sazhin, A. & Flint, M. (1992) The microplankton organisms at the oxic-anoxic interface in the pelagial of the Black Sea. *FEMS Microbiology Letters*, 101, 245–250.

SUPPORTING INFORMATION

Additional supporting information can be found online in the Supporting Information section at the end of this article.

How to cite this article: Louca, S., Taylor, G.T., Astor, Y.M., Buck, K.N. & Muller-Karger, F.E. (2022) Transport-limited reactions in microbial systems. *Environmental Microbiology*, 1–15. Available from: https://doi.org/10.1111/1462-2920.16275

14622920, 0, Downloaded from https://sfamjournals.onlinelibrary.wiley.com/doi/10.1111/1462-2920.16275 by University Of Oregon, Wiley Online Library on [21/11/2022]. See the Terms and Conditions (https://onlinelibrary.wiley.com/terms-and-conditions) on Wiley Online Library for rules of use; OA articles are governed by the applicable Creative Commons License

Transport-limited reactions in microbial systems
- Supplementary Material -

Stilianos Louca[1,2,*], Gordon T. Taylor[3], Yrene M. Astor[4], Kristen N. Buck[5] & Frank E. Muller-Karger[5]

[1]Department of Biology, University of Oregon, USA
[2]Institute of Ecology and Evolution, University of Oregon, USA
[3]School of Marine and Atmospheric Sciences, Stony Brook University, USA
[4]Estación de Investigaciones Marinas de Margarita, Fundación La Salle de Ciencias Naturales, Punta de Piedras, Estado Nueva Esparta, Venezuela
[5]College of Marine Science, University of South Florida, USA
[*]Corresponding author

S.1 Why equilibrium cannot be guaranteed when some reactions are non-reversible

Here we explain why reversibility of all reactions is generally needed for guaranteeing that reactions are always at (local) thermodynamic equilibrium, when infinitely fast (or, equivalently, when given sufficient time to equilibrate). Since this discussion refers to local reaction dynamics, we henceforth focus on well-mixed systems, or equivalently, systems without any spatial extent. In a numerical context, this means that we are considering the reaction dynamics in a single grid cell in discretized space.

We consider a set of R reactions involving M metabolites, with stoichiometric matrix $\mathbb{S} \in \mathbb{R}^{M\times R}$. We denote by $\mathbf{h}(t) \in \mathbb{R}^R$ the vector listing reaction rates at time t, by $\mathbf{C}(t)$ the vector listing metabolite concentrations at time t, and $\mathbf{C}_o \in \mathbb{R}^M$ the vector listing the initial metabolite concentrations. Hence we have $\mathbf{C}(t) = \mathbf{C}_o + \mathbb{S}\cdot\mathbf{H}(t)$, where we defined $\mathbf{H}(t) := \int_0^t \mathbf{h}(s)\, ds$ as the total reaction flux until time t. We call any function $\mathbf{h} : [0,\infty) \to \mathbb{R}^R$ an "exergonic trajectory" if at all times $t \geq$ each reaction either has rate 0 or is exergonic (i.e., only exergonic reactions are performed), and we call a "dead-end state" any state $\mathbf{C} \in \mathbb{R}^M$ at which none of the reactions are exergonic. Hence, exergonic trajectories represent plausible dynamics of a biologically catalyzed dissimilatory reaction system, in which microbes only perform a reaction if the reaction can yield energy for growth [1], while dead-end states correspond to chemical conditions in which none of the reactions can yield any energy for growth. Note that once an exergonic trajectory reaches a dead-end state, all rates become zero thereafter. We are interested in the following question: Are dead-end states reached by exergonic trajectories always guaranteed to be equilibrium states, i.e., in which all reactions are at thermodynamic equilibrium? As explained below, the answer is no.

If some reactions are non-reversible, the dead-end state reached by an exergonic trajectory need not necessarily constitute a thermodynamic equilibrium. Indeed, reaching equilibrium would mean that the limit $\mathbf{C}(\infty)$ is an equilibrium, which would mean that the following system of algebraic equations is satisfied:

$$\mathbb{S}^{\mathrm{T}} \cdot \ln(\mathbf{C}_o + \mathbb{S}\cdot\mathbf{H}(\infty)) = \ln(\mathbf{K}), \tag{1}$$

where $\mathbf{K} \in \mathbb{R}^R$ is the vector listing the equilibrium constants of all reactions. There is no guarantee that all entries of $\mathbf{H}(\infty)$ can be made non-negative while solving Eq. (1), and hence in the presence of non-reversible reactions there need not exist an exergonic trajectory leading to equilibrium.

As a simple example, consider the situation where two biologically catalyzed redox reactions share a common product: The oxidation of hydrogen sulfide (H_2S) with oxygen and the oxidation of sulfide with nitrate via denitrification ($NO_3^- \rightarrow N_2$) can both produce SO_4^{2-}. If O_2 is initially abundant while NO_3^- is rare, it is in principle possible that the first reaction leads to such a rapid and strong accumulation of SO_4^{2-} that the second reaction (which is not known to be biologically reversible) becomes endergonic.

S.2 Pseudocode description of the FRT approach

The following pseudocode outlines the FRT approach discussed in the main text, for n spatial dimensions ($n \in \{1, 2, 3\}$).

Notation and terminology: For brevity, we call "metabolite" any reactant or product of a modeled reaction (including H^+, H_2O etc). The concentrations of some metabolites may be strongly determined/buffered by non-modeled abiotic reactions; for example, H^+ concentrations are by definition determined by pH, which is in turn strongly influenced by a myriad of processes that are hard to account for in a reaction-transport model (or may simply not be of particular interest). Similarly, H_2O should generally be considered to have constant activity (1) even if it is consumed/produced by some reactions. To accommodate such situations, we allow the prior specification of concentrations for a subset of metabolites, so that these metabolites are not influenced by the modeled reactions but nevertheless enter the thermodynamic calculations where necessary. For example, in our Cariaco model we set pH as well as H_2O and CO_2 concentrations to typical values in the Cariaco Basin. We henceforth refer to such metabolites as "background" metabolites, to distinguish them from "tracked" metabolites, i.e., metabolites whose concentrations are not known a priori and whose dynamics are to be predicted by the reaction-transport model.

For simplicity, we focus on the case where all of the fast reactions are non-reversibly catalyzed. We denote real time by $t \geq 0$ and spatial location by $x \in \mathbb{R}^n$. Let M and M^{b} be the number of tracked and background metabolites, respectively. Let the vector $\mathbf{C} \in \mathbb{R}^M$ represent the concentrations of all tracked metabolites and $\mathbf{C}^{\mathrm{b}} \in \mathbb{R}^{M^{\mathrm{b}}}$ represent the concentrations of all background metabolites. Let R and $\overline{R}$ be the number of fast and slow (kinetically limited) reactions, respectively. Let the vector $\mathbf{h} \in \mathbb{R}^R$ denote the rates of fast reactions, and $\overline{\mathbf{h}} \in \mathbb{R}^{\overline{R}}$ denote the rates of slow reactions. We use $\mathcal{L}$ to denote the linear differential operator that encodes physical transport dynamics in the reaction-transport partial differential equations; for example, in the case of diffusive and advective transport we have $\mathcal{L}[C_m] = \nabla \cdot (\mathbb{D}_m \nabla C_m - \mathbf{v}_m C_m)$, where $\mathbb{D}_m$ is the diffusivity and v_m the advection speed for metabolite m. Note that $\mathbb{D}_m$ and v_m may be time- and space-dependent, in which case $\mathcal{L}$ is also time- and space-dependent.

Pseudocode

Input: Stoichiometric matrix $\mathbb{S} \in \mathbb{R}^{M \times R}$ of fast reactions, restricted to tracked metabolites.
Input: Stoichiometric matrix $\mathbb{S}^{\mathrm{b}} \in \mathbb{R}^{M^{\mathrm{b}} \times R}$ of fast reactions, restricted to background metabolites.
Input: Stoichiometric matrix $\overline{\mathbb{S}} \in \mathbb{R}^{M \times \overline{R}}$ of slow reactions, restricted to tracked metabolites.
Input: Kinetic laws for slow reactions, i.e., specifying how $\overline{\mathbf{h}}$ depends on local metabolite concentrations, as well as other given environmental parameters (e.g., temperature and pressure).
Input: Time interval δ between successive fast reaction stages.
Input: Total real time T covered by the simulation.

Input: Spatial domain $\Omega \subseteq \mathbb{R}^n$ and associated discrete spatial grid G.
Input: Physical transport dynamics for each tracked metabolite m and at each $(t, x) \in [0, T] \times \Omega$, for example in the form of diffusivities $\mathbb{D}_m(t, x)$ and advection speeds $\mathbf{v}_m(t, x)$.
Input: Initial concentrations for each tracked metabolite in each spatial grid cell at time 0, i.e., $\mathbf{C}(0, x)$ for all $x \in \Omega$.
Input: Boundary conditions (concentrations or fluxes) for each tracked metabolite at each boundary point $x \in \partial\Omega$ and each time point $t \in [0, T]$.
Input: Known concentrations for all background metabolites, i.e., $\mathbf{C}^{\mathrm{b}}(t, x)$ for all $(t, x) \in [0, T] \times \Omega$.
Output: Predicted metabolite concentrations $\mathbf{C}(t, x)$ as a function of time $t \in [0, T]$ and space $x \in \Omega$.

Set $t = 0$.
while $t < T$ **do**
    # Transport & slow reaction stage
    Solve the following system of slow-reaction-transport differential equations, from time t to $t + \delta$:

$$\frac{\partial \mathbf{C}}{\partial t} = \overline{\mathbb{S}} \cdot \overline{\mathbf{h}} + \mathcal{L}[\mathbf{C}]. \tag{2}$$

    # Run fast reaction stage in each spatial grid cell
    for each grid cell $g \in G$ **do**
        Initialize $\tilde{\mathbf{C}}(0) \leftarrow \mathbf{C}(t + \delta, x_g)$, where $x_g \in \Omega$ is the center of grid cell g.
        Solve the fast reaction differential equations until reaching a dead end, without advancing t:

$$\frac{\partial \tilde{\mathbf{C}}}{\partial s} = \mathbb{S} \cdot \mathbf{h}(s). \tag{3}$$

        # Here, the rates $\mathbf{h}(s)$ are computed based on $\tilde{\mathbf{C}}(s)$ and $\mathbf{C}^{\mathrm{b}}(t, x_g)$, as described in Section S.3.
        Adopt $\mathbf{C}(t + \delta, x_g) \leftarrow \tilde{\mathbf{C}}(\infty)$, i.e., set $\mathbf{C}$ to the reached dead end in each grid cell.
    end for
    Advance real time: $t \leftarrow t + \delta$
end while

Note that the slow-reaction-transport differential equation (2) can in principle be solved with any standard elliptic PDE solver, such as MATLAB's `pdepe`. The same limitations and requirements (e.g., regarding initial conditions, boundary conditions, spatial grid resolution, time step) apply here as in standard reaction-transport models. Similarly, the fast-reaction differential equation (3) can be solved with common solvers, such as MATLAB's `ode45`.

S.3 Details on the thermodynamically driven reaction rates

In this section we explain how we implemented the fast reaction stage within any given spatial grid cell. For simplicity, we focus on the case where all fast reactions are non-reversibly catalyzed.

Notation: We denote by s the "pseudotime" during a single fast reaction stage, keeping in mind that pseudotime units during this stage are infinitely smaller than real time units; hence, pseudotime s advances without advancing real time. We henceforth call any reactant or product of a reaction a "metabolite" for brevity. As before, we distinguish between "tracked" metabolites (i.e., metabolites whose concentrations are not known a priori and whose dynamics are to be predicted by the reactions-transport model) and "background" metabolites (i.e., metabolites whose concentrations are known/specified beforehand, such as H_2O and H^+). We

denote by $\mathcal{M}$ the set of tracked metabolites, by $\mathcal{M}^{\mathrm{b}}$ the set of background metabolites, by $M := |\mathcal{M}|$ the number of tracked metabolites, by $M^{\mathrm{b}} := |\mathcal{M}^{\mathrm{b}}|$ the number of background metabolites, by $\mathbb{S} \in \mathbb{R}^{M \times R}$ the stoichiometric matrix of the fast reactions restricted to tracked metabolites, by $\mathbb{S}^{\mathrm{b}} \in \mathbb{R}^{M^{\mathrm{b}} \times R}$ the stoichiometric matrix of the fast reactions restricted to background metabolites, by $\tilde{\mathbf{C}} \in \mathbb{R}^{M}$ the vector listing the concentrations of tracked metabolites (e.g., in $\mathrm{mol} \cdot \mathrm{L}^{-1}$) in a given spatial grid cell, by $\mathbf{C}^{\mathrm{b}} \in \mathbb{R}^{M^{\mathrm{b}}}$ the vector listing the concentrations of all background metabolites in the same grid cell, and by $\mathbf{h} \in \mathbb{R}^{R}$ the vector listing the rates of all R fast reactions (e.g., in $\mathrm{mol} \cdot \mathrm{L}^{-1} \cdot \mathrm{d}^{-1}$) in that grid cell. For any reaction r, we denote by ΔG_r its Gibbs free energy, which generally depends on current metabolite concentrations, temperature and pressure. We denote by $\Delta G_r^{\mathrm{m}} \leq 0$ the maximum Gibbs free energy at which reaction r can proceed. Such a threshold can account, for example, for minimum energy requirements for ATP synthesis [2, 3], and is sometimes referred to as "biological energy quantum" [4, 5] or "critical free energy" [6].

Dynamics: During the fast reaction stage, the reaction rates $\mathbf{h}$ influence the M explicitly tracked metabolite concentrations as follows:

$$\frac{d\tilde{\mathbf{C}}}{ds} = \mathbb{S} \cdot \mathbf{h}, \tag{4}$$

while $\mathbf{C}^{\mathrm{b}}$ remains constant. Before we explain precisely how the rates $\mathbf{h}$ are determined as a function of the current $\tilde{\mathbf{C}}$, we mention that for each catalyzed reaction r we set $h_r = 0$ whenever its Gibbs free energy is $\geq \Delta G_r^{\mathrm{m}}$. Recall that:

$$\Delta G_r = \Delta G_r^o + R_{\mathrm{g}} T \sum_{m \in \mathcal{M}} \mathbb{S}_{mr} \ln(\tilde{C}_m) + R_{\mathrm{g}} T \sum_{m \in \mathcal{M}^{\mathrm{b}}} \mathbb{S}^{\mathrm{b}}_{mr} \ln(C^{\mathrm{b}}_m), \tag{5}$$

where R_{g} is the universal gas constant, T is temperature, and ΔG_r^o is the reaction's standard Gibbs free energy at the local temperature and pressure. Let K_r denote the reaction's equilibrium constant (at the local temperature and pressure). Note that K_r (by definition) is related to ΔG_r^o as follows:

$$0 = \Delta G_r^o + R_{\mathrm{g}} T \ln(K_r), \tag{6}$$

thus:

$$\ln(K_r) = -\frac{\Delta G_r^o}{R_{\mathrm{g}} T}. \tag{7}$$

It thus follows that $\Delta G_r < \Delta G_r^{\mathrm{m}}$ if and only if:

$$\sum_{m \in \mathcal{M}} \mathbb{S}_{mr} \ln(\tilde{C}_m) < \ln(K_r^*) + \frac{\Delta G_r^{\mathrm{m}}}{R_{\mathrm{g}} T}. \tag{8}$$

where we defined:

$$\ln(K_r^*) := \ln(K_r) - \sum_{m \in \mathcal{M}^{\mathrm{b}}} \mathbb{S}^{\mathrm{b}}_{mr} \ln(C^{\mathrm{b}}_m). \tag{9}$$

The new quantity K_r^* can be interpreted as an equilibrium constant restricted to the tracked metabolites, given the known and fixed concentrations of background metabolites in the focal grid cell. In particular, K_r^* only depends on K_r and on the a priori specified concentrations $\mathbf{C}^{\mathrm{b}}$, but not on $\tilde{\mathbf{C}}$. For each fast reaction $r \in \{1, .., R\}$, we define the deviation between the current chemical state and thermodynamic equilibrium

as follows:

$$f_r(\tilde{\mathbf{C}}) := \sum_{m \in \mathcal{M}} \mathbb{S}_{mr} \ln(\tilde{C}_m) - \ln(K_r^*). \tag{10}$$

Then, each reaction r will only proceed if:

$$f_r(\tilde{\mathbf{C}}) < \frac{\Delta G_r^{\mathrm{m}}}{R_{\mathrm{g}} T}. \tag{11}$$

To ensure that a dead end (where none of the reactions can proceed) is rapidly reached in the fast reaction stage, by default we set the r-th reaction rate proportional to $-f_r(\tilde{\mathbf{C}})$, specifically:

$$h_r(\tilde{\mathbf{C}}) := -\alpha \cdot \frac{f_r(\tilde{\mathbf{C}})}{|\ln(K_r^*)|}, \tag{12}$$

whenever $f_r(\tilde{\mathbf{C}}) < 0$, where $\alpha > 0$ is a proportionality constant. Hence, the more exergonic a reaction is, the faster it proceeds. The reason for dividing each f_r by $|\ln(K_r^*)|$ is that this rescaling ensures that f_r is roughly of unit scale for all fast reactions, which improves the robustness of numerical integration. We thus obtain the following autonomous system of M differential equations:

$$\frac{d\tilde{\mathbf{C}}}{ds} = \mathbb{S} \cdot \mathbf{h}(\tilde{\mathbf{C}}(s)), \quad \text{where} \quad h_r(\tilde{\mathbf{C}}) := \max\left(0, -\alpha \cdot \frac{f_r(\tilde{\mathbf{C}})}{|\ln(K_r^*)|}\right). \tag{13}$$

The above system is numerically integrated forward in pseudotime, separately for each grid cell until a dead end is reached. This dead end is then taken as the new concentration vector in that grid cell, which is used as an input to the subsequent slow-reaction-transport stage. Note that the value of the proportionality constant α theoretically does not influence the reached dead ends, and may be chosen in a way convenient for numerical ODE solvers. Through experimentation, we found that the following choice worked well:

$$\alpha := \frac{1}{R} \sum_{r=1}^{R} \left| \left(\mathbb{S}^+ \cdot \tilde{\mathbf{C}}(0) \right)_r \right|, \tag{14}$$

where $\mathbb{S}^+$ is the Moore-Penrose pseudoinverse of $\mathbb{S}$.

S.4 Investigating the robustness to relative kinetics

The thermodynamically driven kinetics during the fast reaction stage, described in Supplement S.3, while numerically convenient, is only one of many similarly plausible choices. Indeed, all that the FRT assumes is that in each small spatial grid cell all or a subset of reactions proceed until "completion" (i.e., until they are exergonic, or at equilibrium if reversible) at much shorter time scales that physical mixing across space, however no particular assumption is made regarding the relative rates at which various fast reactions take place. To investigate the sensitivity of FRT predictions to the relative rates of fast reactions, we also performed simulations of the Cariaco Basin model where the rate of each reaction during the fast reaction stage was determined based on mass-action kinetics, i.e., as follows:

$$h_r(\tilde{\mathbf{C}}) = \kappa_r \prod_{m \in \mathcal{L}_r} \tilde{C}_m. \tag{15}$$

Here, $\mathcal{L}_r \subseteq \mathcal{M}$ is the set of tracked metabolites that are considered potentially limiting for reaction r; in our analysis $\mathcal{L}_r$ comprised the electron donor and electron acceptor of reaction r. Thus, reaction rates were assumed to follow 1st order kinetics with respect to each electron donor and acceptor, which is plausible since in the FRT limit reactions are generally substrate-limited. In particular, the above mass-action kinetics replace the thermodynamically driven kinetics in Eq. (13). The coefficients κ_r were randomly and independently chosen within the interval $[0.01, 1]$, uniformly on a logarithmic scale. Note that only the relative values of $\kappa_1, \kappa_2, ..$ matter, since fast reactions all occur in pseudotime while real time is fixed. We repeated our simulations with 100 alternative random combinations of the $\kappa_1, \kappa_2, ..$, and compared the predicted metabolite concentration profiles across space and time to those predicted from the thermodynamically driven kinetics from Supplement S.3.

We found that the concentrations predicted based on mass-action kinetics closely resembled the predictions based on thermodynamically driven kinetics. Specifically, the average Pearson correlation (i.e., averaged over all simulations) between the two types of predictions was 0.998 for NH_4^+ (standard deviation 0.0016), 0.981 for NO_3^- (s.d. 0.013), 0.740 for NO_2^- (s.d. 0.38), 0.993 for O_2 (s.d. 0.0029), 0.999 for H_2S (s.d. 0.00009), 0.999 for CH_4 (s.d. 0.0007), 0.991 (s.d. 0.0035) for N_2 and 0.999 (s.d. 0.00089) for SO_4^{2-}. Hence, for all metabolites except for NO_2^-, mass-action kinetics predicted practically identical concentrations as the thermodynamically driven kinetics.

The somewhat lower agreement between the two approaches with respect to NO_2^- is not surprising and not a major concern, for the following reason: NO_2^- generally only occurs in trace quantities (often below detection limit) in the Cariaco Basin water column, presumably due to its rapid consumption by processes such as nitrification and/or anammox. Indeed, all models correctly predicted that most of the produced NO_2^- is rapidly consumed, and predicted concentrations were close to zero ($\ll 1\ \mu\mathrm{M}$), consistent with the data. However, such predictions (i.e., resulting from the difference between two nearly-equal quantities, production minus consumption, each varying at much greater orders of magnitude) are inevitably quite noisy in terms of variations relative to the mean. Overall, the above results reveal that in the FRT limit the relative rates of the various fast reactions had only minor effects on the overall predictions of the model.

S.5 Mean travel time of a diffusing particle

In the following we provide a formula for the expected travel time of a particle diffusing across a one-dimensional interval $[0, L]$. We claim no primacy of the mathematics, so this material is merely provided in support of our other discussions. Suppose that the particle starts at the right boundary ($z = L$) and diffuses within the interval according to Brownian motion with constant diffusivity D, reflecting at the right boundary until it reaches the left boundary ($z = 0$) for the first time. The expected time until this happens, denoted E, can be computed as follows:

$$E = \int_0^\infty dt \int_0^L dz\ \rho(t, z), \tag{16}$$

where $\rho(t, z)$ denotes the probability density of the particle's location at time t and location z [7, Supplement S.2]. This probability density satisfies the following boundary value problem:

$$\frac{\partial \rho}{\partial t} = D\frac{\partial^2 \rho}{\partial z^2}, \quad \rho(t, 0) = 0, \quad \frac{\partial \rho}{\partial z}(t, L) = 0, \quad \rho(0, z) = 2\delta(z - L), \tag{17}$$

where δ denotes the Dirac distribution and the factor 2 is used to account for the fact that "half" of the particle is on the other side of the boundary. Equivalently, we can also compute ρ as the solution to the following

modified boundary value problem on the interval $[0, 2L]$:

$$\frac{\partial \rho}{\partial t} = D\frac{\partial^2 \rho}{\partial z^2}, \quad \rho(t,0) = 0, \quad \rho(t,2L) = 0, \quad \rho(0,z) = 2\delta(z-L). \tag{18}$$

The solution to Eq. (18) is well-known [e.g. 8, Section 5.13.1]:

$$\rho(t,z) = \frac{2}{L}\sum_{n=1}^{\infty} \sin\left(\frac{\pi n}{2}\right) \cdot \sin\left(\frac{\pi n}{2L}z\right) \cdot \exp\left[-Dt\left(\frac{\pi n}{2L}\right)^2\right]. \tag{19}$$

Inserting Eq. (19) into Eq. (16) yields:

$$\begin{aligned} E =& \frac{2}{L}\sum_{n=1}^{\infty} \sin\left(\frac{\pi n}{2}\right) \cdot \int_0^{\infty} dt \exp\left[-Dt\left(\frac{\pi n}{2L}\right)^2\right] \int_0^L dz\ \sin\left(\frac{\pi n}{2L}z\right) \\ =& \frac{2}{L}\sum_{n=1}^{\infty} \sin\left(\frac{\pi n}{2}\right) \cdot \frac{4L^2}{D\pi^2 n^2} \cdot \frac{2L}{\pi n}\left[1 - \cos\left(\frac{\pi n}{2}\right)\right] \\ =& \frac{16L^2}{D\pi^3}\sum_{n=1}^{\infty} \frac{1}{n^3} \cdot \sin\left(\frac{\pi n}{2}\right) \cdot \left[1 - \cos\left(\frac{\pi n}{2}\right)\right] \\ =& \frac{16L^2}{D\pi^3}\sum_{n=1}^{\infty} \frac{1}{n^3} \cdot \sin\left(\frac{\pi n}{2}\right) = \frac{16L^2}{D\pi^3}\sum_{k=0}^{\infty} \frac{(-1)^k}{(2k+1)^3}. \end{aligned} \tag{20}$$

The series $\sum_{k=0}^{\infty} \frac{(-1)^k}{(2k+1)^3}$ is equal to $\pi^3/32$ [9], hence we obtain the expected travel time:

$$\boxed{E = \frac{L^2}{2D}.} \tag{21}$$

As a first realistic example, we consider a typical marine sediment column, where redox gradients typically span one or more meters [1] (for example, the sulfate-methane transition zone is typically around one or more meters below the water-sediment interface [10–12]). Molecular diffusivities for sulfate and methane in marine sediments are typically in the order of 2–4 $\times\ 10^{-5}\ \mathrm{m}^2 \cdot \mathrm{day}^{-1}$. Choosing $L = 1\mathrm{m}$ and $D = 3 \times 10^{-5}\ \mathrm{m}^2 \cdot \mathrm{day}^{-1}$ yields an expected diffusive travel time of $E \approx 16700$ days or about 46 years.

As a second example, we consider a hypothetical water column similar to the Cariaco Basin (depths 180–900 m), where eddy diffusion is thought to be the dominant mode of transport for dissolved nutrients. The eddy diffusivity in this zone was previously estimated by [7] within the approximate range of $170 - -1050\,\mathrm{m}^2 \cdot \mathrm{day}^{-1}$, although we mention that substantial differences exist between the top and bottom regions. Assuming an average diffusivity of $D = 600\mathrm{m}^2 \cdot \mathrm{day}^{-1}$, we obtain an expected diffusive travel time of $E \approx 430$ days, a bit longer than a year. For reference, more accurate calculations accounting for the depth-dependence of the eddy diffusivity in Cariaco (as described in [7, Supplement S.2]) yield an expected travel time of 3.0 years.

S.6 A precise criterion for the separation of time scales

In the following we more precisely discuss a criterion for the separation of time scales between reaction rates and physical transport. The general idea is that such a separation of time scales is given when reacting molecules spend much more time traveling from the region of production to the region of consumption than

they spend inside the region of consumption. Since this discussion inevitably depends on the details of the system a hand (system geometry, reaction kinetics, transport dynamics etc), here we focus on a simple but in our view sufficiently illuminating example. Our discussion extends previous material by Louca *et al.* [7, Supplement S4]. We consider the case of a single reaction in a one-dimensional sediment or water column, where sulfide diffusing upwards from the bottom boundary is oxidized using oxygen diffusing downwards from the top boundary (depth 0). For simplicity, we assume that oxygen and sulfide are the only possibly limiting substrates, that the diffusivity of each substrate is constant across space and time, that the reaction rate is of first order in each substrate's concentration (i.e., proportional to the product $[H_2S] \cdot [O_2]$) and that the system has reached steady state, so that aerobic sulfide oxidation occurs in a restricted zone (henceforth "transition zone") at some intermediate depth, where both sulfide and oxygen overlap. We also assume that the O_2 concentration decreases approximately linearly with depth from the top boundary until reaching zero at the bottom end of the transition zone, at depth L. Let l denote the width of the transition zone. The narrower the transition zone is relative to L, the more separated the reaction- and transport-time scales will be and the closer the system will be to being transport-limited. Indeed, the average time spent by an oxygen molecule traveling from the top boundary to the transition zone relative to the time spent inside that zone increases as l/L decreases.

We can also express the ratio l/L in terms of reaction kinetic parameters and transport parameters. Let A_o denote the concentration of O_2 at the top boundary, κ the 1st order reaction constant (so that the rate of sulfide consumption is $\kappa \cdot [H_2S] \cdot [O_2]$), and D the diffusivity of sulfide. Under the above assumptions, we obtain the following depth profile for the sulfide concentration [7, Supplemental Eq. 41]:

$$B(y) = B(0) \cdot 3^{\frac{2}{3}} \Gamma(2/3) \cdot \mathrm{Ai}\left(\sqrt[3]{\frac{\kappa A_o}{DL}} \cdot y\right), \tag{22}$$

where $B(y)$ is the sulfide concentration at distance y above the point where oxygen disappears, Γ is the Gamma function and Ai is the Airy function of the first kind. We operationally define as the width of the transition zone (l) as the distance at which B drops to half of its value, i.e. $B(l) = B(0)/2$. Solving for l yields:

$$l \approx 0.76 \cdot \sqrt[3]{\frac{DL}{\kappa A_o}}. \tag{23}$$

Let τ be the hypothetical half-life time of a sulfide molecule, when subjected to oxygen concentration A_o (i.e., under aerobic conditions encountered at the top boundary), i.e. $\tau = \ln(2)/\kappa A_o$. Substituting for τ in Eq. (23) yields:

$$l \approx 0.86 \cdot \sqrt[3]{D\tau L}. \tag{24}$$

Thus, the condition $l/L \ll 1$ is equivalent to $0.86 \cdot \sqrt[3]{D\tau L} \ll L$, which is equivalent to:

$$\tau \ll 1.6 \cdot \frac{L^2}{D}. \tag{25}$$

Recall that L^2/D is twice the expected time E that it would take a diffusing sulfide molecule to traverse interval $[0, L]$ (Supplement S.5). Hence, condition (25) translates to:

$$\boxed{\frac{\tau}{E} \ll 3.2.} \tag{26}$$

In other words, a separation of time scales is given if the half-life time of a sulfide molecule under aerobic conditions is much shorter than 3 times its expected travel time between the transition zone and the top boundary.

S.7 Nondimensionalization of reaction-transport equation

In the following we present a nondimensionalized version of the reaction-transport equation (1) introduced in the main article. We assume that our system has a "characteristic" spatial scale X spanned by redox gradients (e.g., the typical distance between different redox zones), a characteristic transport time scale τ (the typical travel time of substrates from their zone of production or influx to their zone of consumption) and a characteristic metabolite concentration G (e.g., the maximum concentration of any limiting substrate within the system). For example, in the case of aerobic sulfide oxidation along a 1-dimensional water or sediment column discussed in Supplement S.6, X could be the distance between the transition zone and the upper boundary, τ would be the expected travel time of a diffusing molecule between the transition zone and the upper boundary, G would be the oxygen concentration at the top boundary (or sulfide concentration at the bottom boundary). Note that it is also possible to consider a different characteristic scale along each spatial dimension and a different characteristic concentration for each metabolite, however this would substantially complicate the discussion and is thus omitted below.

We define the unitless (rescaled) concentrations $\overline{C}_m := C_m/G$, the unitless space variables $\overline{\mathbf{x}} := \mathbf{x}/X$, the unitless time variable $\overline{t} := t/\tau$, the unitless diffusivities $\overline{\mathbb{D}}_M := (\tau/X^2)\cdot\mathbb{D}_m$, the unitless advection velocities $\overline{\mathbf{v}}_m := (\tau/X)\cdot\mathbf{v}_m$. Written in these new variables, Eq. (1) in the main article becomes:

$$\frac{G}{\tau}\frac{\partial\overline{C}_m}{\partial\overline{t}} = \sum_r \mathbb{S}_{mr}h_r + \frac{G}{X}\overline{\nabla}\cdot\left(\frac{X^2}{X\tau}\overline{\mathbb{D}}_m\overline{\nabla C}_m - \frac{X}{\tau}\overline{\mathbf{v}}_m\overline{C}_m\right), \tag{27}$$

where $\overline{\nabla}$ is the Nabla operator with respect to $\overline{\mathbf{x}}$. Thus:

$$\frac{\partial\overline{C}_m}{\partial\overline{t}} = \frac{\tau}{G}\sum_r \mathbb{S}_{mr}h_r + \overline{\nabla}\cdot\left(\overline{\mathbb{D}}_m\overline{\nabla C}_m - \overline{\mathbf{v}}_m\overline{C}_m\right). \tag{28}$$

For purposes of argumentation, we consider the case of first-level kinetics:

$$h_r = \kappa_r \prod_{m\in L_r} C_m = \frac{1}{\tau\prod_{m'\in L_r} G}\overline{\kappa}_r \prod_{m\in L_r} G\overline{C}_m = \frac{1}{\tau}\overline{\kappa}_r \prod_{m\in L_r}\overline{C}_m, \tag{29}$$

where we defined the unitless reaction coefficient $\overline{\kappa}_r := \kappa_r\cdot\frac{\tau}{G}\prod_{m'\in L_r} G$. Combining Eqs. (29) and (28) yields the nondimensionalized reaction-transport equations:

$$\boxed{\frac{\partial\overline{C}_m}{\partial\overline{t}} = \sum_r \mathbb{S}_{mr}\overline{\kappa}_r \prod_{m\in L_r}\overline{C}_m + \overline{\nabla}\cdot\left(\overline{\mathbb{D}}_m\overline{\nabla C}_m - \overline{\mathbf{v}}_m\overline{C}_m\right).} \tag{30}$$

For simplicity, suppose that $\mathbb{D}_m$ and $\mathbf{v}_m$ are constant in space and time, and that $\mathbb{D}_m$ is a diagonal matrix (as is typically the case). A separation of time scales between reaction rates and physical transport translates to the condition that $\overline{\kappa}_r \gg \overline{\mathbb{D}}_m^{ii}$ and $\overline{\kappa}_r \gg \overline{\mathbf{v}}_m^i$ (or equivalently, $1/\overline{\kappa}_r \ll 1/\overline{\mathbb{D}}_m^{ii}$ and $1/\overline{\kappa}_r \ll 1/\overline{\mathbf{v}}_m^i$), for every spatial dimension i. The ratio $1/\overline{\kappa}_r$ can be loosely interpreted as the expected time it takes for a given substrate molecule to be consumed by reaction r, if all other limiting substrates are at concentration G, relative to the

characteristic time scale τ. The ratio $1/\overline{\mathbb{D}}_m^{ii}$ can be interpreted as the expected time that a molecule would take to traverse the distance $2X$ along the i-th spatial dimension due to diffusion, relative to the characteristic time scale τ (see Supplement S.5). Similarly, the ratio $1/\overline{\mathbf{v}}_m^i$ can be interpreted as the expected time that a molecule would take to traverse the distance X along the i-th spatial dimension due to advection, relative to the characteristic time scale τ. Hence, a separation of time scales translates to the condition that the expected life time of a reacting molecule (under conditions of high substrate concentrations) is much shorter than the typical time scales involved in the traversal of the system's spatial scale X.

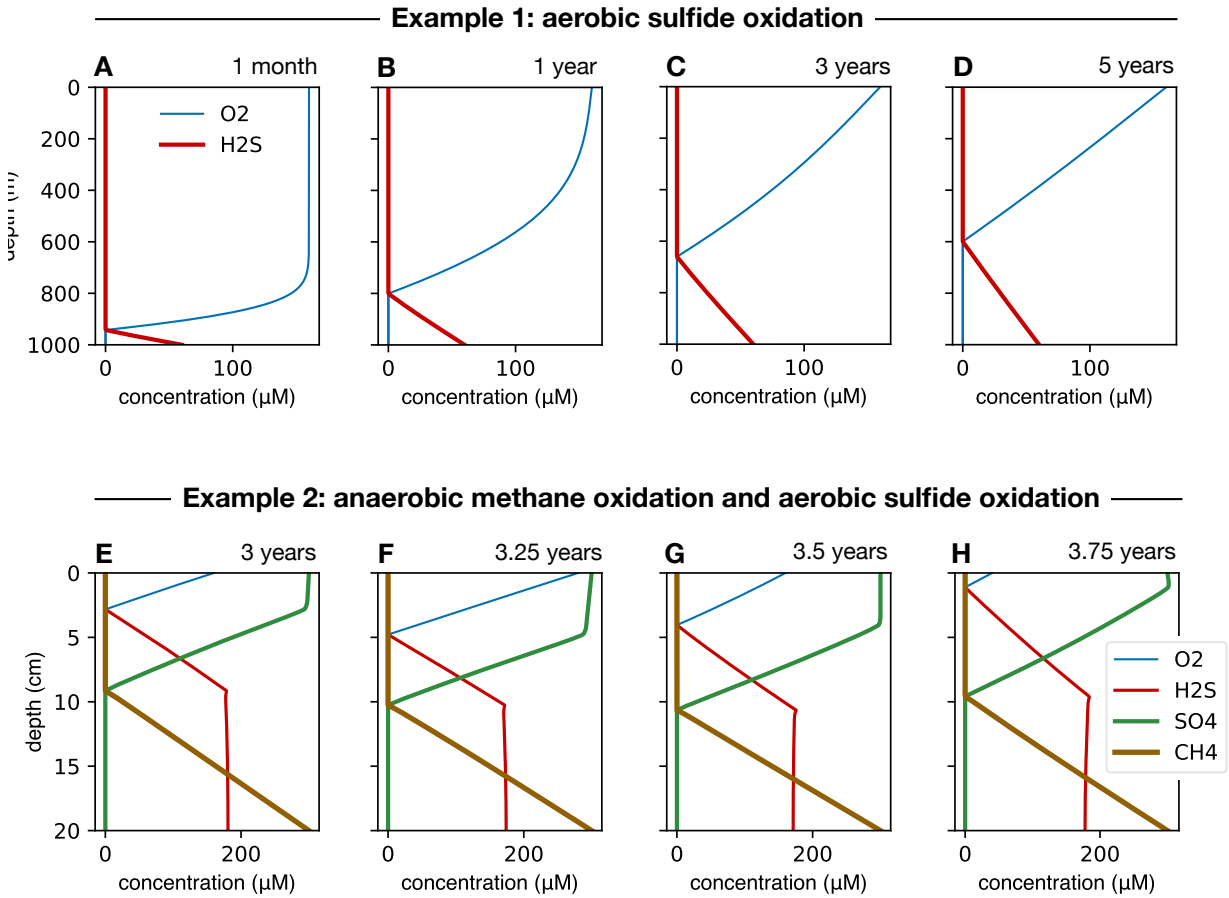

Figure S1: **Concentration depth profiles predicted by example models.** (A-D) Concentration depth profiles for O_2 and H_2S, predicted by the 1st example FRT model (aerobic sulfide oxidation in a water column, Figs. 2A–C in the main text) 1 month, 1 year, 3 years and 5 years after the onset of the simulation. Note that the depth profiles eventually stabilize such that the steady state fluxes of O_2 and H_2S into the reaction front (at the sulfide-oxygen interface) have a ratio of 2:1. (E–H) Concentration depth profiles for O_2, H_2S, SO_4^{2-} and $CH4$, predicted by the 2nd example FRT model (anaerobic methane oxidation and aerobic sulfide oxidation in a sediment column, Figs. 2D–F in the main text) 3 years, 3.25 years, 3.5 years and 3.75 years after the onset of the simulation. Note that in this model two reaction fronts quickly form, however their precise depth oscillates due to seasonal variations of oxygen concentrations at the sediment-water interface.

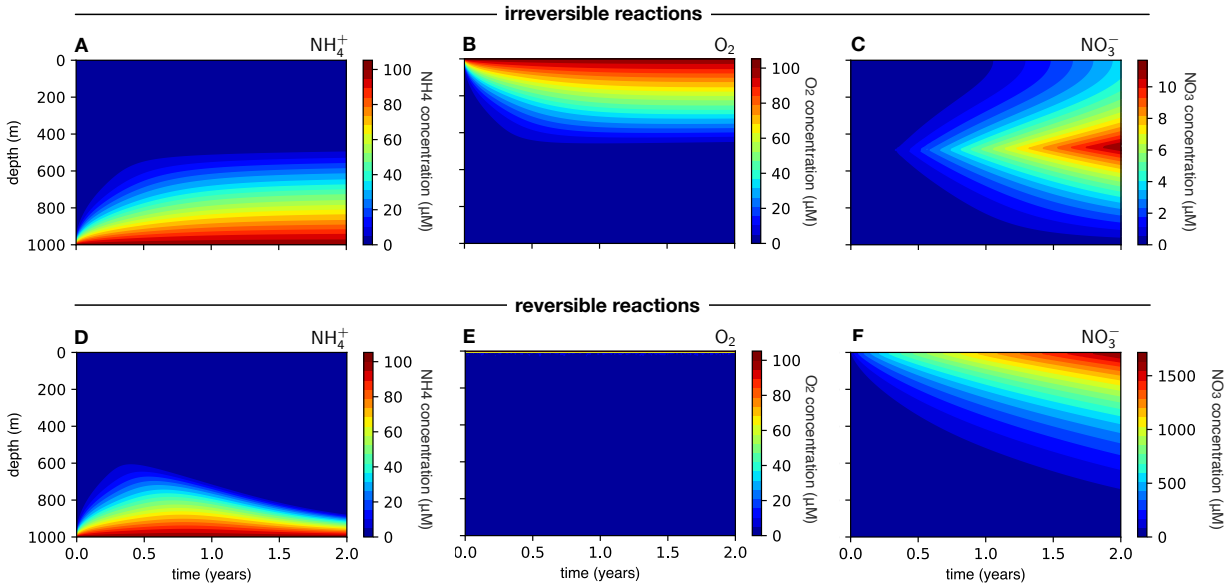

Figure S2: **Nitrification & anammox (irreversible vs. reversible reactions).** Simulations of a system of 3 fast reactions (the two nitrification steps and anammox) across a poorly mixed water column in the FRT limit, while either assuming that all reactions are non-reversibly catalyzed (top row) or assuming that all reactions are reversible (and thus always at equilibrium, bottom row). Each figure shows the predicted concentration of either $\mathrm{NH4}^+$, O_2 or NO_3^-, over depth and time. Observe the strong differences between the predictions of the two models. In the reversible reaction model, anammox proceeds in the reverse direction near the upper boundary, i.e., producing NH_4^+ and NO_2^- from N_2, thus leading to drastically different dynamics than in the (more biologically plausible) irreversible reaction model.

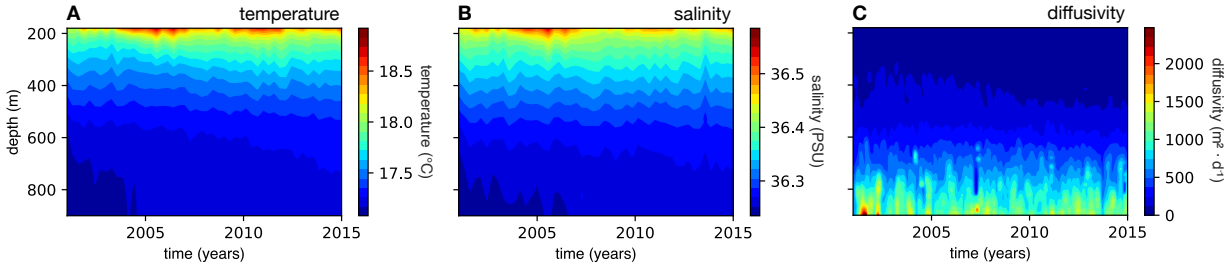

Figure S3: **Cariaco Basin physical variables.** (A) Temperature and (B) salinity measured in the Cariaco Basin water column, across depth and time [13]. (C) Vertical eddy diffusivity, previously estimated using the buoyancy frequency and salinity profiles [7].

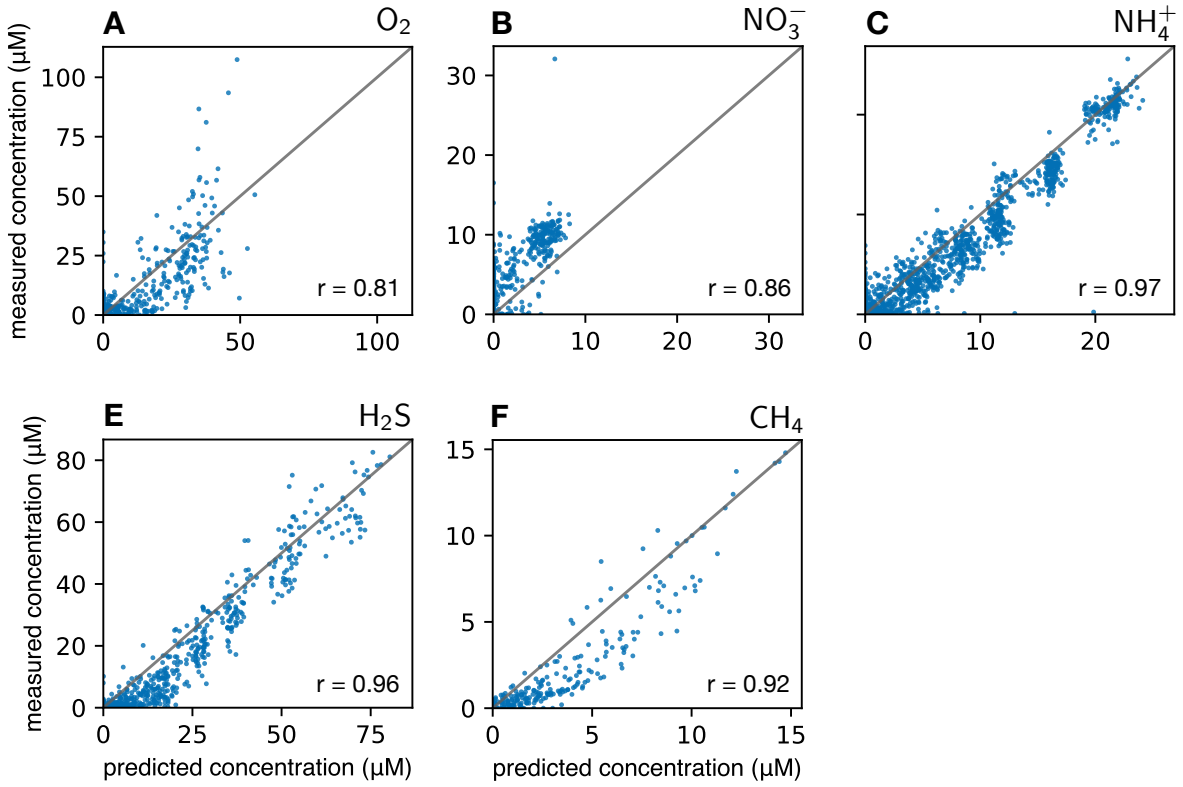

Figure S4: Metabolite concentrations predicted by the Cariaco Basin FRT model (horizontal axes) compared to concentrations measured at the same depth and time (vertical axes). The diagonal lines are shown for reference. Pearson correlations (r) are written in the figures (all were statistically significant, $P < 0.01$).

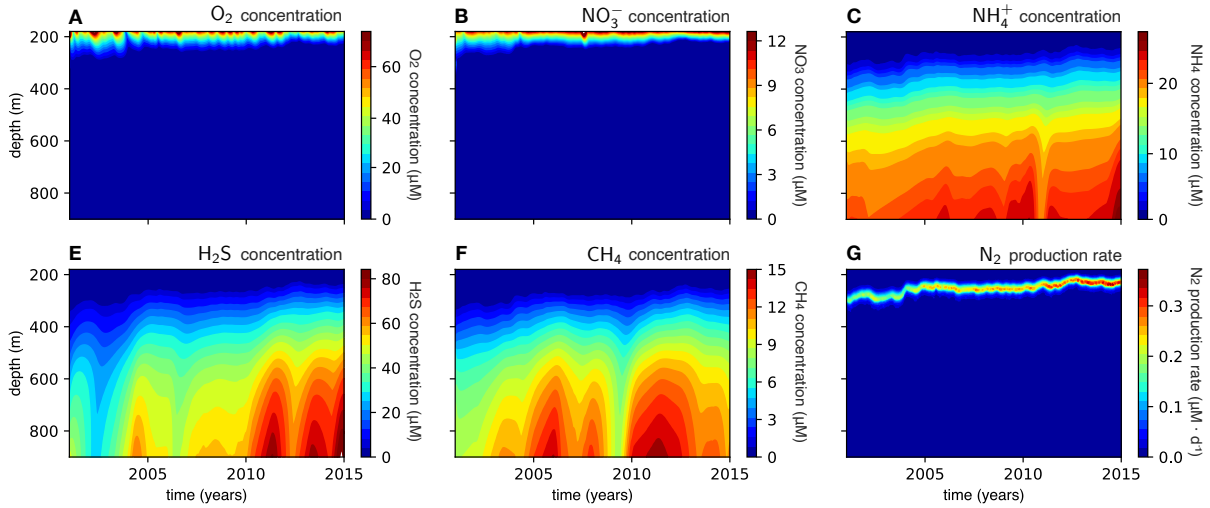

Figure S5: Concentrations of dissolved O_2, NO_3^-, NH_4^+, H_2S and CH_4, as well as rates of N_2 production (fixed nitrogen loss), predicted by the FRT model when temperature and vertical eddy diffusivity were kept constant in time (at each depth set to their temporal average at that depth).

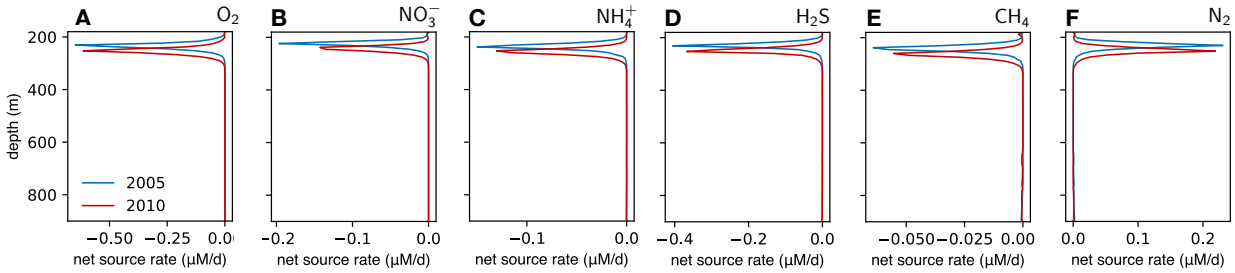

Figure S6: **Cariaco Basin predicted net sources.** Net metabolite production/consumption rate profiles across depth, predicted using the Cariaco Basin FRT model for years 2005 and 2010 (January 1st). Negative rates represent a net consumption, positive rates represent a net production.

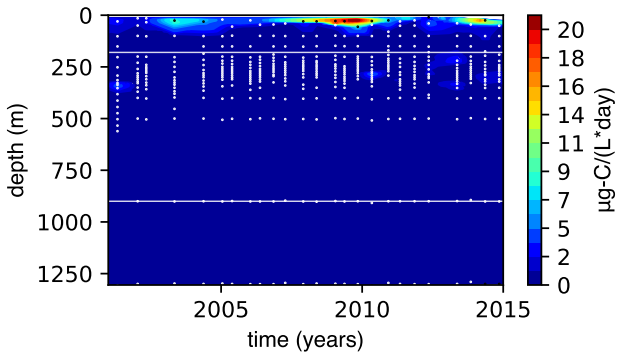

Figure S7: Bacterial heterotrophic production rates measured in the Cariaco Basin water column (carbon assimilated per volume per time). Black or white dots indicate original data points; contour plots are obtained via linear interpolation.

References

[1] Canfield DE, Thamdrup B. Towards a consistent classification scheme for geochemical environments, or, why we wish the term 'suboxic' would go away. Geobiology. 2009; 7:385–392.

[2] Jin Q, Bethke CM. A new rate law describing microbial respiration. Applied Environmental Microbiology. 2003; 69:2340–2348.

[3] Jin Q, Bethke CM. Predicting the rate of microbial respiration in geochemical environments. Geochimica et Cosmochimica Acta. 2005; 69:1133–1143.

[4] Schink B. Energetics of syntrophic cooperation in methanogenic degradation. Microbiology and Molecular Biology Reviews. 1997; 61:262–280.

[5] Hoehler TM. Biological energy requirements as quantitative boundary conditions for life in the subsurface. Geobiology. 2004; 2:205–215.

[6] Jackson BE, McInerney MJ. Anaerobic microbial metabolism can proceed close to thermodynamic limits. Nature. 2002; 415:454–456.

[7] Louca S, Astor YM, Doebeli M, Taylor GT, Scranton MI. Microbial metabolite fluxes in a model marine anoxic ecosystem. Geobiology. 2019; 17:628–642.

[8] Herman R. A Course in Mathematical Methods for Physicists (Boca Raton, FL, USA: CRC Press, 2013).

[9] Sun ZW. A new series for π^3 and related congruences. International Journal of Mathematics. 2015; 26:1550055.

[10] Wilms R, Sass H, Köpke B, Cypionka H, Engelen B. Methane and sulfate profiles within the subsurface of a tidal flat are reflected by the distribution of sulfate-reducing bacteria and methanogenic archaea. FEMS Microbiology Ecology. 2007; 59:611–621.

[11] Treude T, Krause S, Maltby J, Dale AW, Coffin R, Hamdan LJ. Sulfate reduction and methane oxidation activity below the sulfate-methane transition zone in Alaskan Beaufort Sea continental margin sediments: Implications for deep sulfur cycling. Geochimica et Cosmochimica Acta. 2014; 144:217–237.

[12] Cao C, Cai F, Qi H, Zhao S, Wu C. Differences in the sulfate–methane transitional zone in coastal pockmarks in various sedimentary environments. Water. 2021; 13:68.

[13] Muller-Karger FE, Astor YM, Benitez-Nelson CR, Buck KN, Fanning KA, Lorenzoni L, *et al.* The scientific legacy of the CARIACO ocean time-series program. Annual Review of Marine Science. 2019; 11:5.1–5.25.